INSIHGT: Accessible multimodal systems biology with quantitative molecular phenotyping in 3D

Chun Ngo Yau,[1,2†] Jacky Tin Shing Hung,[1,2†] Thomas Chun Yip Wong[1,2], Bei Huang,[1,3] Ben Tin Yan Wong,[1,2] King Ngai Chow,[1,2] Eldric Pui Lam Tsoi,[1,2] Yuqi Tan,[4] Joshua Jing Xi Li[5], Yun Kwok Wing,[1,3] Hei Ming Lai,[1,2,6*]

Affiliations

[1]Department of Psychiatry, Faculty of Medicine, The Chinese University of Hong Kong, Shatin, Hong Kong SAR, China.

[2]Li Ka Shing Institute of Health Sciences, Faculty of Medicine, The Chinese University of Hong Kong, Shatin, Hong Kong SAR, China.

[3]Li Chiu Kong Family Sleep Assessment Unit, Department of Psychiatry, The Chinese University of Hong Kong, Shatin, Hong Kong SAR, China.

[4]Department of Microbiology and Immunology, Stanford University School of Medicine, Stanford, California, USA.

[5]Department of Pathology, School of Clinical Medicine, The University of Hong Kong, Queen Mary Hospital.

[6]Department of Chemical Pathology, Faculty of Medicine, The Chinese University of Hong Kong, Shatin, Hong Kong SAR, China.

[†]Equal contributions

[*]Corresponding author. Email: hmlai@cuhk.edu.hk

Summary

Biological systems are complex, encompassing intertwined spatial, molecular and functional features. However, methodological constraints always limit the completeness of information that can be extracted. Here, we report the development of INSIHGT, a minimally perturbative and cost-efficient three-dimensional (3D) spatial biology method utilizing superchaotropes and host-guest chemistry. This allows quantitative, highly multiplexed and multi-modal readout of tissue biomolecules in up to centimeter-scale biological systems. Diverse antigens, mRNA transcripts, neurotransmitters, and post-translational and epigenetic modifications, are well-preserved and visualized, allowing multi-round molecular probing for high-dimensional spatial biology and compatibility with downstream traditional histology. With INSIHGT, we mapped previously undescribed podocyte-to-parietal epithelial cell microfilaments and demonstrated their geodesic clustering in mouse glomeruli, catalogued sparsely located neurofilament-intensive inclusion bodies in the human cerebellum, and identified NPY-proximal cell types defined by spatial morpho-proteomics in mouse hypothalamus. We anticipate INSIHGT can form the foundations for 3D spatial multi-omics technology development and holistic systems biology studies.

Keywords: INSIHGT, 3D histology, spatial biology, multi-omics, tissue clearing

Introduction

The complexity of biological systems mandates high-dimensional measurements to obtain an integrative understanding. However, measurements are inevitably perturbative. Spatially resolved transcriptomics and highly multiplexed immunohistochemistry (IHC) have proven to be powerful approaches to extract spatial molecular insights from tissue slices, but the two-dimensional (2D) readout limits the representativeness of the information extracted. Meanwhile, three-dimensional (3D) multiplexed visualization of tissue structural and molecular features can reveal previously unknown organization principles. However, despite significant advances in optical tissue clearing technologies [1], which promises to reveal the authentic 3D nature of tissue architecture and molecular distributions, the achievable depths of probe penetration limits the depth of analysis. [2]. Above all, the limited penetration of antibodies in 3D immunohistochemistry (IHC) represents the most significant barrier to 3D spatial biology [2].

In recent years, multiple creative solutions have been proposed [3–6] . However, an accessible technology that balances the authenticity and volume of data extracted is still lacking. For example, signal homogeneity across penetration depth is suboptimal with most methods, where probes preferentially deposit near the tissue surface, complicating quantitative protein expression determination. These shortcomings hinder the wide adoption of 3D tissue analysis in research and renders them unsatisfactory for clinical translation.

To address these technical bottlenecks, we report the development of *In situ Host-Guest* Chemistry for *T*hree-dimensional Histology (INSIHGT). INSIHGT is a user-friendly 3D histochemistry method, featuring (1) homogeneous probe penetration up to centimeter depths,

(2) producing quantitative, highly specific immunostaining signals, (3) a fast and affordable workflow to accommodate different tissue sizes and shapes, (4) immersion-based staining, thus easily adopted in any laboratory and ready for scaling and automate, and (5) uses off-the-shelf antibodies or probes and is directly applicable to otherwise unlabelled mouse and human tissues fixed with paraformaldehyde only. INSIHGT was developed based on the manipulation of chemical potential gradients that drive diffusiophoresis using an *in situ* supramolecular reaction system. Specifically, a boron cluster compound *closo*-dodecahydrododecaborate $[B_{12}H_{12}]^{2-}$ [7] and a γ-cyclodextrin derivative were used to achieve switchable modulation of probe motions throughout the tissue and attain homogeneous, deeply penetrating 3D histochemistry. As the first report on the application of supramolecular chemistry [8] and boron clusters [9] in 3D histology and systems biology [10], our work also opened further avenues for trans-disciplinary research.

Results

Reconceptualizing biomolecular transport phenomena reveals weakly coordinating superchaotropes as non-denaturing protein solubilizers

The limited penetration of macromolecular probes in complex biological systems belongs to the broader subject of transport phenomena, where diffusion and advections respectively drive the dissipation and directional drift of mass, energy and momentum. When biomolecules such as proteins are involved, the (bio)molecular fluxes are additionally determined by binding reactions, which can significantly deplete biomolecules due to their high binding affinities and low concentrations employed. However, a general approach to tune biomolecular binding affinities while preserving protein stability is lacking. Therefore, most deep staining methods involve enhancing diffusive and advective flux to boost probe mobility and hence penetration. These measures, although performed satisfactorily, add complexity to the method and limits their generality, scalability, and data authenticity.

Since advective engineering usually requires specialized equipment, we limited ourselves to engineering reaction-diffusion of macromolecular probes in a tissue matrix (**Fig. 1A**), which expresses the concentration of species **c** at space coordinates **q** and time *t* as

$$\frac{\partial \mathbf{c}(\mathbf{q},t)}{\partial t} = -\nabla \cdot (D\nabla \mathbf{c}(\mathbf{q},t)) - R(\mathbf{q},t),$$

where D is the Fick's diffusivity matrix driven by the concentration gradient $\nabla \mathbf{c}$. For biomolecules, the reaction and diffusion processes often strongly affect each other, and there are many non-specific interactions with solvents, co-solutes and tissue components that depend on the specific context. Importantly, the numbers of each biomolecular species are usually conserved in a reaction-diffusion process. It is therefore advantageous to consider them as a unified propagative process, which is captured by the Maxwell-Stefan diffusivity matrix $\mathcal{D}$ (**Fig. 1A**), driven by spatial chemical potential gradients $\nabla \boldsymbol{\mu}$ as

$$\frac{\partial \mathbf{c}(\mathbf{q},t)}{\partial t} = -\nabla \cdot (\mathcal{D}\nabla \mu(\mathbf{q},t)).$$

The above formulation describes discrete, instantaneous binding reactions as multicomponent diffusion processes (**Fig. 1A**). An important result from the above conceptual paradigm shift is the equivalence of biomolecular association and desolvation, which suggests that using co-solutes to solubilize proteins can promote deep penetration by disfavouring other reaction-diffusion trajectories, such as binding to their fixed tissue targets. However, known solubilizers such as chaotropes and detergents are only weakly effective, while at higher concentrations they often denature proteins through direct interactions with proteins (**Fig. 1B, C**). We hence focus on testing weakly coordinating superchaotropes (WCS), which should solubilize proteins while preserving their functions (**Fig. 1B, C**). We identified a target list of weakly coordinating ions based on their utility in isolating extremely electrophilic species for X-ray crystallography, or as conjugate bases of superacids. After the solubilization stage has homogeneously distributed macromolecules through the tissue matrix, measures must be taken to negate the superchaotropicity to reinstate inter-biomolecular interactions in a bio-orthogonal and system-wide manner. With the enthalpy-driven chaotropic assembly reaction, we postulated the activities of superchaotropes can be effectively negated with supramolecular hosts in situ, reactivating interactions between the macromolecular probes and their tissue targets.

Based on the above theoretical analyses, we designed a scalable deep molecular phenotyping method, performed in two stages: a first infiltrative stage where macromolecular probes co-diffuse homogeneously with WCS with minimized reaction barriers, followed by the addition of macrocyclic compounds for in situ host-guest reactions, altering the chemical potential landscapes to redirect macromolecular probes to their tissue targets. With a much-narrowed list of chemicals to screen, we first benchmarked the performances of several putative WCS host-guest systems using a standard protocol (**Fig. S1**). These include perrhenate/α-cyclodextrin (ReO_4^-/αCD), ferrocenium/βCD ($[Fe(C_5H_5)_2]^+$/βCD), *closo*-dodecaborate ions ($[B_{12}X_{12}]^{2-}$/γCD (where X = H, Cl, Br, or I)), metallacarborane ($[Co(7,8\text{-}C_2B_9H_{11})_2]^-$/γCD), and polyoxometalates ($[PM_{12}O_{40}]^{3-}$/γCD (where M = Mo, or W)) (**Fig. 1D-E**). Group 5 and 6 halide clusters and rhenium chalcogenide clusters such as $[Ta_6Br_{12}]^{2+}$, $[Mo_6Cl_{14}]^{2-}$ and $\{Re_6Se_8\}^{2+}$ derivatives were excluded due to instability in aqueous environments. Only ReO_4^-, $[B_{12}H_{12}]^{2-}$, and $[Co(7,8\text{-}C_2B_9H_{11})_2]^-$ proved compatible with immunostaining conditions without causing tissue destruction or precipitates. $[B_{12}H_{12}]^{2-}$/γCD produced the best staining sensitivity, specificity and signal homogeneity across depth (**Fig. S2**), while the effect of derivatizing γCD was negligible (**Fig. S2**). We chose the more soluble 2-hydroxypropylated derivative (2HPγCD) for its higher water solubility in our applications.

In-situ host-guest chemistry for three-dimensional histology (INSIHGT)

After establishing the biomolecular compatibility of the $[B_{12}H_{12}]^{2-}$-2HPγCD system, we developed INSIHGT - a minimally perturbative, scalable, deeply and homogeneously penetrating method for 3D histology that balances the authenticity and volume of data extracted. INSIHGT involves simply incubating the tissue in $[B_{12}H_{12}]^{2-}$/PBS with antibodies, then in 2HPγCD/PBS (**Fig. 2A**). The whole process involves only simple incubations, is compatible with conventionally formaldehyde-fixed tissues, and requires no specialized equipment. It is also the

fastest deep immunolabelling from tissue harvesting to image (**Fig. 2E**). We compared INSIHGT with other 3D IHC techniques using a stringent benchmarking experiment (see **Methods, Fig. S1**) to compare their penetration depths and homogeneity [2]. For eFLASH [11] and SWITCH-ELAST [12], due to the lack of specialized equipment, only their binding kinetics control buffers were employed and the external force fields or mechanically-induced tissue dimension changes were omitted. We found INSIHGT achieved the deepest immunolabeling penetration with the best signal homogeneity throughout the penetration depth (**Fig. 2B**). To quantitatively compare the signal, we segmented the labelled cells and compared the ratio between the deep immunolabelling signal and the reference signal against their penetration depths. Exponential decay curve fitting showed that the signal homogeneity was near-ideal (**Fig. 2C, Table S1**) - where there was negligible decay in deep immunolabelling signals across the penetration depth. We repeated our benchmarking experiment with different markers, and by correlating INSIHGT signal with the reference signal, we found INSIHGT provides reliable quantitative mapping of cellular marker expression levels throughout an entire mouse hemi-brain stained for 1 day (**Fig. 2D**). Hence, with excellent penetration homogeneity and scalability, INSIHGT can be the ideal method for mapping whole organs with cellular resolution.

Notably, after washing, only negligible $[B_{12}H_{12}]^{2-}$ will remain within the tissue. This is evident as the cut-staining intensity profile of INSIHGT was similar to that of iDISCO (**Fig. S3**) which has identical tissue pre-processing steps. Upon the addition of 2HPγCD and washing off the so-formed complexes, the penetration enhancement effect was completely abolished. This suggests that $[B_{12}H_{12}]^{2-}$ and cyclodextrins do not further permeabilize or disrupt the delipidated tissue.

High-throughput, multiplexed, dense whole organ mapping

We applied INSIHGT to address the challenges in whole organ immunostaining, where the limited penetration of macromolecular probes hinders the scale, speed, or choice of antigens that can be reliably mapped, while the use of aggressive permeabilization can lead to antigen destruction. Due to the operational simplicity, scaling up the sample size in organ mapping experiments with INSIHGT is thus straightforward and can be done using multiwell cell culture plates (**Fig. 3A**), which we demonstrated the case by mapping 14 mouse kidneys in parallel (**Fig. 3B, Fig. S4**) within 6 days of tissue harvesting.

We then exemplify the capability of INSIHGT to simultaneously map densely expressed targets in whole organs (**Fig. 3C-I**). We first performed multiplexed staining on mouse kidney with 3 days of incubation for LEL, PNA, GSL, and AQP-1, which are targets associated with poor probe penetration (**Fig. 3C-D**). We then proceeded to map a 36-months old whole mouse brain over 3 days of staining for Calbindin, NeuN, and c-Fos, providing cell type and activity information across the aged organ (**Fig. 3E-I**). With whole organ sampling, we identified regions where ageing related changes were prominent, these include cavitations in the bilateral thalamus and striatum (**Fig. 3G-H**), as well as calbindin-positive deposits in the stratum radiatum of hippocampus (**Fig. 3I**). Interestingly, there seems to be an increased c-Fos expression level

among the neurons surrounding thalamic cavitations (**Fig. 3G**) which are located deep within the brain tissue and thus cannot be explained by preferential antibody penetration, suggesting these cavitations may affect baseline neuronal activities.

Overall, INSIHGT overcomes technical, operational, and cost bottlenecks towards accessible organ mapping for every basic molecular biology laboratory, providing rapid workflows to qualitatively evaluate organ-wide structural, molecular, and functional changes in health and disease, regardless of the spatial density of the visualization target.

Boron cluster-based supramolecular histochemistry as a foundation for spatial multi-omics

With the maturation of single-cell omics technologies, integrating these high-dimensional datasets becomes problematic. Embedding these data in their native 3D spatial contexts is the most biologically informative approach. Hence, we next tested whether our boron cluster supramolecular chemistry allows the retention and detection of multiple classes of biomolecules and their features, based on which 3D spatial multi-omics technologies can be developed.

With identical tissue processing steps and INSIHGT conditions, we tested 357 antibodies and found 323 of them (90.5%) produced the expected immunostaining patterns (**Fig. 4A, Fig. S5-7, Table S2**). This was at least six times the number of compatible antibodies demonstrated by any other deep immunostaining method (**Fig. 4A**), demonstrating the robustness and scalability of INSIHGT. Antigens ranging from small molecules (e.g., neurotransmitters with chiral specificity), epigenetic modifications, peptides to proteins and their phosphorylated forms were detectable using INSIHGT (**Fig. 4B-C**). The specificity of immunostaining even allowed the chirality of neurotransmitters (e.g., L-Glu versus D-Glu), the degree of lysine methylations (i.e., mono-, di- and tri-methylation) and the symmetricity of arginine dimethylations to be distinguished from one another (**Fig. 4B-C**). We further tested 21 lectins to detect complex glycosylations, proving that $[B_{12}H_{12}]^{2-}$ do not sequester divalent metal ions essential for their carbohydrate recognition (**Fig. 4D, Fig. S8**).

Small molecule dyes such as nucleic acid probes, which are mostly positively charged, presents a separate challenge as they precipitate with *closo*-dodecaborates, forming $[\text{probe}]^{n+}/[B_{12}H_{12}]^{2-}$ precipitates when co-applied with INSIHGT. We found size-matched and charge-complementing cyclodextrin derivatives as cost-effective supramolecular host agents for non-destructive deep tissue penetration and preventing precipitation. For example, sulfobutylether-βCD (SBEβCD) (**Fig. 4E**) can react with nucleic acid probes to form [probe⊂SBEβCD], which exhibits penetration enhancement during INSIHGT (**Fig. 4F, G**) without precipitation problems.

Finally, single-molecule fluorescent in situ hybridization (FISH) is also applicable for co-detection of protein antigens and RNAs with INSIHGT. Combining all the above probes, simultaneous 3D visualization of protein antigens, RNA transcripts, protein glycosylations, epigenetic modifications, and nuclear DNA is possible using a mixed supramolecular system in conventionally formalin-fixed intact tissue (**Fig. 4H**). Taken together, our results suggest *in situ* boron cluster supramolecular histochemistry can form the foundation for volumetric spatial

multi-omics method development.

Centimeter-scale 3D histochemistry by isolated diffusional propagation

Since antibody penetration remains the most challenging obstacle, we focus the remainder of our investigation on larger-scale 3D immunophenotyping. We thus applied INSIHGT to visualize centimeter-scale human brain samples, without using any external force fields to drive the penetration of macromolecular probes. These large, pigmented samples were sliced in the middle of the tissues' smallest dimensions to allow imaging of the deepest areas with tiling confocal microscopy. We show that INSIHGT can process a 1.5 cm × 1.5 cm × 3 cm human cortex block for parvalbumin (PV) (**Fig. 5A–C**), with excellent homogeneity and demonstration of parvalbumin neurons predominantly in layer 4 of the human cortex.

We further scaled INSIHGT to a 1.75 cm × 2.0 cm × 2.2 cm human cerebellum block for blood vessels (using *Griffonia simplicifolia lectin I, GSL-I*) (**Fig. 5D–F**), again revealing excellent homogeneity with no decay of signal across the centimeter of penetration depth. This shows that the use of boron cluster-based host-guest chemistry remains applicable for highly complex environments at the centimetre scale. The results further show that macromolecular transport within a dense biological matrix can remain unrestricted in a non-denaturing manner by globally adjusting inter-biomolecular interactions.

Volumetric spatial morpho-proteomic cartography for cell type identification and neuropeptide proximity analysis

We next extended along the molecular dimension on conventionally fixed tissues, where highly multiplexed immunostaining-based molecular profiling in 3D had not been accomplished previously. A single round of INSIHGT-based indirect immunofluorescence plus lectin histochemistry can simultaneously map up to 6 antigens (**Fig. S9**), tolerating a total protein concentration at >0.5 μg/μl in the staining buffer, and is limited only by spectral overlap and species compatibility. To achieve higher multiplexing, antibodies can be stripped off with 0.1 M sodium sulfite in the $[B_{12}H_{12}]^{2-}$-containing buffer after overnight incubation at 37°C (**Fig. 6A**). Since $[B_{12}H_{12}]^{2-}$ does not significantly disrupt intramolecular and intermolecular noncovalent protein interactions, the approach can be directly applied to routine formaldehyde-fixed tissues, we observed no tissue damage and little distortion, obviating the need for additional or specialist fixation methods.

We exemplified this approach by mapping 28 neuronal marker expression levels in a 2 mm-thick hypothalamus slice over 7 imaging rounds (**Fig. 6A–C**). With each iterative round taking 48 hours (including imaging, retrieval and elution), the whole manual process from tissue preparation to the 28-plex image took 16 days. After registration and segmentation using Cellpose 2.0 [13] (**Fig. 6D, E**), we obtained 192,075 cells and their differentially expressed proteins (DEPs) based on immunostaining signals. Uniform manifold approximation and projection (UMAP) analysis of a subset of 84,139 cells based on 50 markers (omitting 3 blood vessels channels and separately accounting for signal mean intensity and standard deviations, **Fig. 6F, Fig. S10-11**) plus their distance to the nearest vessels revealed 42 cell type clusters,

allowing their 3D spatial interrelationships to be determined (**Fig. S12**).

3D spatial proteomics can blend morphology and molecular information to infer functional relationships, which is inaccessible to spatial transcriptomics or single-cell multi-omics. Recent characterizations of neuronal network activities based on the diffusional spread of neuropeptides highlight the need for 3D spatial mapping of protein antigens. To obtain these morphological-molecular relationships using INSIHGT, we segmented the neuropeptide Y (NPY)-positive fibers and computed the 3D distance to each UMAP-clustered cell types' somatic membranes (**Fig. 6G–J**). While most clusters have a similar distance from NPY fibers, certain clustered cells (notably right tile clusters 1 and 2) are more proximally associated with NPY fibers, suggesting these cell clusters are differentially modulated by NPY when isotropic diffusion is assumed in the local brain parenchyma. Nonetheless, our dataset and analysis demonstrated it is possible to estimate the likely modulatory influence for a given cell-neuropeptide pair, providing a new approach to discovering novel neuronal dynamics paradigms.

Fine-scale 3D imaging reveals novel intercellular contacts traversing the Bowman space in mouse kidneys

We found that the process of INSIHGT from fixation to completion preserve delicate structures such as free-hanging filaments and podia, enabling fine-scale analysis of compact structures such as the renal glomeruli. We found novel intercellular contacts traversing the Bowman space, which to the best of our knowledge has not been previously described (**Fig. 7A, B**). These filaments are mostly originated from the podocytic surface, although some were also seen to emerge from parietal epithelial cells (PEC). They were numerous and found around the glomerular globe (**Fig. 7C**), with varied in their length, distance from each other, and morphologies (**Fig. 7D, Fig S13**).

We classified these podocyte-to-PEC microfilaments into "reachers" and "stayers", depending on whether they reached the PEC surface or not (**Fig. 7E**). Microfilaments of the reachers-type were more numerous than the stayers-type per glomerulus (**Fig. 7F**). Visually, we noted the emergence of these filaments tended to cluster together, especially for the reachers-type. To quantify such spatial clustering, we calculated the glomerular surface geodesic distances between the podocytic attachment points for each microfilament, which showed an inverse relationship with their path lengths (**Fig. 7G**), and reachers-type filament are geodesically located nearer to each other than the stayers type (**Fig. S14**). This suggests that the emergence of long, projecting microfilaments that reach across the Bowman space is localized on a few hotspots of the glomerular surface. Whether these hotspots of long-reaching microfilaments are driven by signals originated from the podocyte, the glomerular environment underneath, or the overarching PECs may reveal previously unsuspected podocyte physiological responses within their microenvironments.

Sparsely distributed neurofilament inclusions unique to the human cerebellum

We next completely mapped a 3 mm-thick (post-dehydration dimensions) human

cerebellar folium for NF-H, GFAP and blood vessels (**Fig 8A, Fig. S15-16, Movie S1**), with preserved details down to the Bergmann glia fibers, perivascular astrocytic endfeet, and Purkinje cell axons that makes the amenable to 3D orientation analysis and visualization (**Fig. 8B-D, Fig. S16-17**). The detailed visualization of filamentous structures throughout the 3 mm-thickness is in stark contrast to our previous attempts with similar specimen employing sodium dodecyl sulphate delipidation and the iDISCO method, which showed weak NF-H signal in cerebellar sulci and barely visible GFAP signal in cerebellar white matter (**Fig. S15**) due to poor antibody penetration.

We discovered sparsely distributed NF-H-intense inclusions that are easily missed in 2D sectioning and thus remain uncharacterised. We manually traced and identified 1,078 inclusions throughout the entire imaged volume (**Fig. 8E-F**), where they were found in all of the three basic layers of the cerebellar cortex. A typical morphology of one type of these inclusion is a single bright globular inclusion at the sub-Purkinje layer radial location, with an elongated thick fiber extension that coils back and project to the adjacent molecular layer (**Fig. 8E**). However, much more protean morphologies also exist (**Fig. 8E-F, Fig S18**). To capture the morphological and spatial diversities of these inclusions, we obtained their spatial-morphometric statistics (**Fig. S18A**), followed by principal component analysis of the compiled morphometrics such as Sholl analysis and Horton-Strahler number. The results reveal most of these inclusions to be morphologically homogeneous with variations explained largely by their path lengths, with a small subset characterized by much higher branching of the NF-H-intense filaments (**Fig. S18B**).

INSIHGT bridges the gap between 3D histology and traditional 2D pathology in current clinical practice

The bioorthogonal nature of the INSIHGT chemical system underlies its non-destructiveness. To highlight the clinical impact of INSIHGT in addition to 3D imaging of human samples, we found that INSIHGT-processed samples can be retrieved and processed as naïve tissues for traditional 2D histology via paraffin wax embedding and sectioning. Notably, staining qualities of routine hematoxlin and eosin (H&E) and various special stains on the post-INSIHGT processed slides were indistinguishable from the pre-INSIHGT processed slides even by a senior pathologist (**Fig. 8G-H**). In addition to not interfering with downstream clinical processes, the preserved quality of special staining allows for multi-modal cross-validation of 3D fluorescent imaging findings, making INSIHGT the ideal platform choice for next-generation histopathology (**Fig. 8I**). We envision with INSIHGT, quantitative 3D information within clinical specimens can be maximally extracted with high authenticity, and its fast speed promises compatibility with current clinical workflows and constraints, allowing digital pathology and precision medicine to benefit from 3D analysis.

Discussion

The convergence of multiple technological advances has paved the way for the acquisition of large-scale molecular phenotyping datasets at single-cell resolution, most notably single-cell transcriptomics. With a large number of newly discovered cell states, the quest to extend towards

spatially resolved cell phenotyping based on translated and post-translationally expressed biomolecular signatures is paramount to understanding their structural and functional properties in biology.

Scalable, high-resolution 3D tissue mapping provides a powerful approach to further our understanding of these newly identified cell types. By sampling across whole intact samples, 3D histology can deliver unbiased, quantitative, ground-truth data on the spatial distributions of molecules and cell types in their native tissue contexts. However, 3D tissue imaging is yet to be widely adopted despite the increasing accessibility of tissue clearing, optical sectioning microscopy, and coding-free image processing software. This is due to the limited penetration of probes that plague the field regardless of the combinations of these technologies employed, yielding variable, surface-biased data with questionable representativeness. Creative approaches have provided solutions to the penetration problem but are limited in their scalability and accessibility [2].

Constrained by the requirements of non-advective approaches and compatibility with off-the-shelf reagents, the development of INSIHGT involved re-examining biomolecular transport and protein stability from the first principles, which led us to identify weakly coordinating superchaotrope and its chemical activity modulation by in situ host-guest reactions to implement our theoretical formulation. With the use of *closo*-dodecaborate and cyclodextrin as an additive in PBS, we solved the bottleneck of 3D histology by providing a cost-efficient, scalable, and affordable approach to quantitatively map multiple molecules in centimeter-sized tissues. With an equivalent tissue processing pipeline to iDISCO, INSIHGT shares the same affordability and scalability while providing much faster processing and greatly improved image quality, due to enhanced antibody penetration depth and homogeneity. Mapping tissue blocks simultaneously in multi-well dishes is easily accomplished in any basic molecular biology laboratory. Such simplicity in operation makes it highly accessible and automatable, as it requires no specialized equipment or skills. Furthermore, cocktails of off-the-shelf antibodies can be directly added to PBS supplemented with $[B_{12}H_{12}]^{2-}$. Finally, we note that both $[B_{12}H_{12}]^{2-}$ salts and cyclodextrins are non-hazardous and stable indefinitely at ambient temperatures [7].

With the affordability and accessibility of INSIHGT, we anticipate its diverse applications in 2D and 3D histology applications. Meanwhile, boron cluster-based supramolecular histochemistry can form the backbone for 3D spatial molecular-structural-functional profiling methods and studies, as well as atlas mapping efforts. The high-depth, quantitative readout of well-preserved tissue biomolecules offered by INSIHGT forms the foundation for multiplexed, multi-modal, and multi-scale 3D spatial biology. By making non-destructive 3D tissue molecular probing accessible, INSIHGT can empower researchers to bridge molecular-structural inferences from subcellular to the organ-wide level. Finally, the compatibility of INSIHGT with downstream traditional 2D histology methods indicates its non-interference with subsequent clinical decision-making. This paves the way for the translation and development of 3D histology-based tissue diagnostics, promising rapid and accurate generation of groundtruth data across entire tissue specimens.

We recognize that INSIHGT still has room for further improvements. Immunostaining penetration homogeneities for larger tissues and denser antigens can be further enhanced, and the penetration of small molecule dyes and lectins were still suboptimal for millimeter-scale tissues. In multi-round immunostaining, we noticed that the staining specificity and sensitivity deteriorated with each round of antibody elution with sulphite or β-mercaptoethanol, calling for a better 3D immunostaining elution method. Alternatively, hyperspectral imaging, nonlinear optics, time-resolved fluorescence techniques, and same-species antibody multiplexing could be explored to extend the multiplexing capabilities of INSIHGT.

Our discovery of boron clusters' capabilities to solubilize proteins globally in a titratable manner, combined with their bio-orthogonal removal with supramolecular click chemistry, can reach beyond histology applications. Given the surprisingly robust performance of INSIHGT in complex tissue environments, we envision they can be applied in simpler *in vitro* settings to control intermolecular interactions – particularly when involving proteins – in a spatiotemporally precise manner.

Acknowledgements: We would like to express our deepest gratitude to the tissue donor and his family for their generosity and wisdom in supporting scientific studies. We thank William Wu for access to confocal microscopy; Cathy Shuk Ling Chan for manual data annotation and analysis; Ka Wai Chan for administrative support to the project. Figure 1 was partly created with BioRender.com.

Funding: The project was supported by the Midstream Research Programme for Universities (MRP/048/20) of the Innovation and Technology Council of Hong Kong, a Direct Grant for Research 2022/23 (2022.072) of the Chinese University of Hong Kong, and the Chinese University of Hong Kong Research Committee Group Research Scheme (GRS) 2021–22.

Author Contributions: Conceptualization: HML. Methodology: HML, CNY, JTSH, TCYW, BTYW, KNC, EPLT. Investigation: HML, CNY, JTSH, TCYW, BH, BTYW, KNC, EPLT, YT, JJXL, YKW. Visualization: HML, CNY, JTSH. Funding acquisition: YKW, HML. Project administration: HML. Supervision: HML. Writing: HML, CNY.

Competing Interests: CUHK filed a patent application in part based on the invention described in this paper with HML and CNY as the inventors.

Data and Materials Availability: Additional experimental data and the custom codes used in this study will be made publicly available upon the acceptance of the manuscript.

References and Notes

1. Zhao, S., Todorov, M.I., Cai, R., -Maskari, R.A., Steinke, H., Kemter, E., Mai, H., Rong, Z., Warmer, M., Stanic, K., *et al.* (2020). Cellular and Molecular Probing of Intact Human Organs. Cell *180*, 796–812.e19.

2. Yau, C.N., Lai, H.M., Lee, K., Kwok, A.J., Huang, J., and Ko, H. (2023). Principles of deep immunohistochemistry for 3D histology. Cell Rep Methods *3*, 100458.

3. Ku, T., Guan, W., Evans, N.B., Sohn, C.H., Albanese, A., Kim, J.-G., Frosch, M.P., and Chung, K. (2020). Elasticizing tissues for reversible shape transformation and accelerated molecular labeling. Nat. Methods *17*, 609–613.

4. Susaki, E.A., Shimizu, C., Kuno, A., Tainaka, K., Li, X., Nishi, K., Morishima, K., Ono, H., Ode, K.L., Saeki, Y., *et al.* (2020). Versatile whole-organ/body staining and imaging based on electrolyte-gel properties of biological tissues. Nat. Commun. *11*, 1982.

5. Lai, H.M., Tang, Y., Lau, Z.Y.H., Campbell, R.A.A., Yau, J.C.N., Chan, C.C.Y., Chan, D.C.W., Wong, T.Y., Wong, H.K.T., Yan, L.Y.C., *et al.* (2022). Antibody stabilization for thermally accelerated deep immunostaining. Nat. Methods *19*, 1137–1146.

6. Mai, H., Luo, J., Hoeher, L., Al-Maskari, R., Horvath, I., Chen, Y., Kofler, F., Piraud, M., Paetzold, J.C., Modamio, J., *et al.* (2023). Whole-body cellular mapping in mouse using standard IgG antibodies. Nat. Biotechnol. 10.1038/s41587-023-01846-0.

7. Pitochelli, A.R., and Hawthorne, F.M. (1960). THE ISOLATION OF THE ICOSAHEDRAL $B_{12}H_{12}^{-2}$ ION. J. Am. Chem. Soc. *82*, 3228–3229.

8. Steed, J.W., and Atwood, J.L. (2013). Supramolecular Chemistry (John Wiley & Sons).

9. Plesek, J. (2002). Potential applications of the boron cluster compounds. 10.1021/cr00010a005.

10. Kitano, H. (2002). Systems biology: a brief overview. Science *295*, 1662–1664.

11. Yun, D.H., Park, Y.-G., Cho, J.H., Kamentsky, L., Evans, N.B., Albanese, A., Xie, K., Swaney, J., Sohn, C.H., Tian, Y., *et al.* (2019). Ultrafast immunostaining of organ-scale tissues for scalable proteomic phenotyping. bioRxiv, 660373. 10.1101/660373.

12. Park, J., Wang, J., Guan, W., Gjesteby, L.A., Pollack, D., Kamentsky, L., Evans, N.B., Stirman, J., Gu, X., Zhao, C., *et al.* (2023). Integrated platform for multi-scale molecular imaging and phenotyping of the human brain. bioRxiv, 2022.03.13.484171. 10.1101/2022.03.13.484171.

13. Pachitariu, M., and Stringer, C. (2022). Cellpose 2.0: how to train your own model. Nat. Methods *19*, 1634–1641.

14. Murray, E., Cho, J.H., Goodwin, D., Ku, T., Swaney, J., Kim, S.-Y., Choi, H., Park, Y.-G.,

Park, J.-Y., Hubbert, A., *et al.* (2015). Simple, Scalable Proteomic Imaging for High-Dimensional Profiling of Intact Systems. Cell *163*, 1500–1514.

15. Renier, N., Wu, Z., Simon, D.J., Yang, J., Ariel, P., and Tessier-Lavigne, M. (2014). iDISCO: A Simple, Rapid Method to Immunolabel Large Tissue Samples for Volume Imaging. Cell *159*, 896–910.

16. Mai, H., Rong, Z., Zhao, S., Cai, R., Steinke, H., Bechmann, I., and Ertürk, A. (2022). Scalable tissue labeling and clearing of intact human organs. Nat. Protoc. *17*, 2188–2215.

17. Voigt, F.F., Kirschenbaum, D., Platonova, E., Pagès, S., Campbell, R.A.A., Kastli, R., Schaettin, M., Egolf, L., van der Bourg, A., Bethge, P., *et al.* (2019). The mesoSPIM initiative: open-source light-sheet microscopes for imaging cleared tissue. Nat. Methods *16*, 1105–1108.

18. Hörl, D., Rojas Rusak, F., Preusser, F., Tillberg, P., Randel, N., Chhetri, R.K., Cardona, A., Keller, P.J., Harz, H., Leonhardt, H., *et al.* (2019). BigStitcher: reconstructing high-resolution image datasets of cleared and expanded samples. Nat. Methods *16*, 870–874.

19. Arshadi, C., Günther, U., Eddison, M., Harrington, K.I.S., and Ferreira, T.A. (2021). SNT: a unifying toolbox for quantification of neuronal anatomy. Nat. Methods *18*, 374–377.

20. Soille, P. Morphological Image Analysis (Springer Berlin Heidelberg).

21. Bigun, J. (1987). Optimal Orientation Detection of Linear Symmetry. 433–438.

22. Khan, A.R., Cornea, A., Leigland, L.A., Kohama, S.G., Jespersen, S.N., and Kroenke, C.D. (2015). 3D structure tensor analysis of light microscopy data for validating diffusion MRI. Neuroimage *111*, 192–203.

23. Bigun, J., Bigun, T., and Nilsson, K. (2004). Recognition by symmetry derivatives and the generalized structure tensor. IEEE Trans. Pattern Anal. Mach. Intell. *26*, 1590–1605.

24. Website Connor Meehan, Jonathan Ebrahimian, Wayne Moore, and Stephen Meehan (2022). Uniform Manifold Approximation and Projection (UMAP) (https://www.mathworks.com/matlabcentral/fileexchange/71902), MATLAB Central File Exchange.

25. Morel, P. (2018). Gramm: grammar of graphics plotting in Matlab. Journal of Open Source Software *3*, 568.

26. Masselink, W., Reumann, D., Murawala, P., Pasierbek, P., Taniguchi, Y., Bonnay, F., Meixner, K., Knoblich, J.A., and Tanaka, E.M. (2019). Broad applicability of a streamlined ethyl cinnamate-based clearing procedure. Development *146*, dev166884.

27. Klingberg, A., Hasenberg, A., Ludwig-Portugall, I., Medyukhina, A., Männ, L., Brenzel, A., Engel, D.R., Figge, M.T., Kurts, C., and Gunzer, M. (2017). Fully automated evaluation of

total glomerular number and capillary tuft size in nephritic kidneys using lightsheet microscopy. J. Am. Soc. Nephrol. *28*, 452–459.

28. Becker, K., Jährling, N., Saghafi, S., Weiler, R., and Dodt, H.-U. (2012). Chemical Clearing and Dehydration of GFP Expressing Mouse Brains. PLoS One *7*, e33916.

29. Jacso, T., Bardiaux, B., Broecker, J., Fiedler, S., Baerwinkel, T., Mainz, A., Fink, U., Vargas, C., Oschkinat, H., Keller, S., *et al.* (2013). The Mechanism of Denaturation and the Unfolded State of the α-Helical Membrane-Associated Protein Mistic. 10.1021/ja408644f.

30. Ganguly, P., Boserman, P., van der Vegt, N.F.A., and Shea, J.-E. (2017). Trimethylamine N-oxide Counteracts Urea Denaturation by Inhibiting Protein–Urea Preferential Interaction. 10.1021/jacs.7b11695.

31. Riddlestone, I.M., Kraft, A., Schaefer, J., and Krossing, I. (2018). Taming the Cationic Beast: Novel Developments in the Synthesis and Application of Weakly Coordinating Anions. Angew. Chem. Int. Ed. *57*, 13982–14024.

32. Lipping, L., Leito, I., Koppel, I., Krossing, I., Himmel, D., and Koppel, I.A. (2015). Superacidity of closo-Dodecaborate-Based Brønsted Acids: a DFT Study. 10.1021/jp506485x.

33. Assaf, K.I., and Nau, W.M. (2018). The Chaotropic Effect as an Assembly Motif in Chemistry. Angew. Chem. Int. Ed Engl. *57*, 13968–13981.

34. Assaf, K.I., Ural, M.S., Pan, F., Georgiev, T., Simova, S., Rissanen, K., Gabel, D., and Nau, W.M. (2015). Water Structure Recovery in Chaotropic Anion Recognition: High-Affinity Binding of Dodecaborate Clusters to γ-Cyclodextrin. Angew. Chem. Int. Ed. *54*, 6852–6856.

35. Karki, K., Gabel, D., and Roccatano, D. (2012). Structure and dynamics of dodecaborate clusters in water. Inorg. Chem. *51*, 4894–4896.

36. Jiang, Y., Cai, Z., Yuan, Q., Cao, W., Hu, Z., Sun, H., Wang, X.-B., and Sun, Z. (2022). Highly Structured Water Networks in Microhydrated Dodecaborate Clusters. J. Phys. Chem. Lett. *13*, 11787–11794.

37. Jiang, Y., Yuan, Q., Cao, W., Hu, Z., Yang, Y., Zhong, C., Yang, T., Sun, H., Wang, X.-B., and Sun, Z. (2022). Unraveling hydridic-to-protonic dihydrogen bond predominance in monohydrated dodecaborate clusters. Chem. Sci. *13*, 9855–9860.

38. Bukovsky, E.V., Peryshkov, D.V., Wu, H., Zhou, W., Tang, W.S., Matthew Jones, W., Stavila, V., Udovic, T.J., and Strauss, S.H. (2017). Comparison of the Coordination of B12F122–, B12Cl122–, and B12H122– to Na+ in the Solid State: Crystal Structures and Thermal Behavior of Na2(B12F12), Na2(H2O)4(B12F12), Na2(B12Cl12), and Na2(H2O)6(B12Cl12). 10.1021/acs.inorgchem.6b02920.

39. Goszczyński, T.M., Fink, K., Kowalski, K., Leśnikowski, Z.J., and Boratyński, J. (2017).

Interactions of Boron Clusters and their Derivatives with Serum Albumin. Sci. Rep. *7*, 9800.

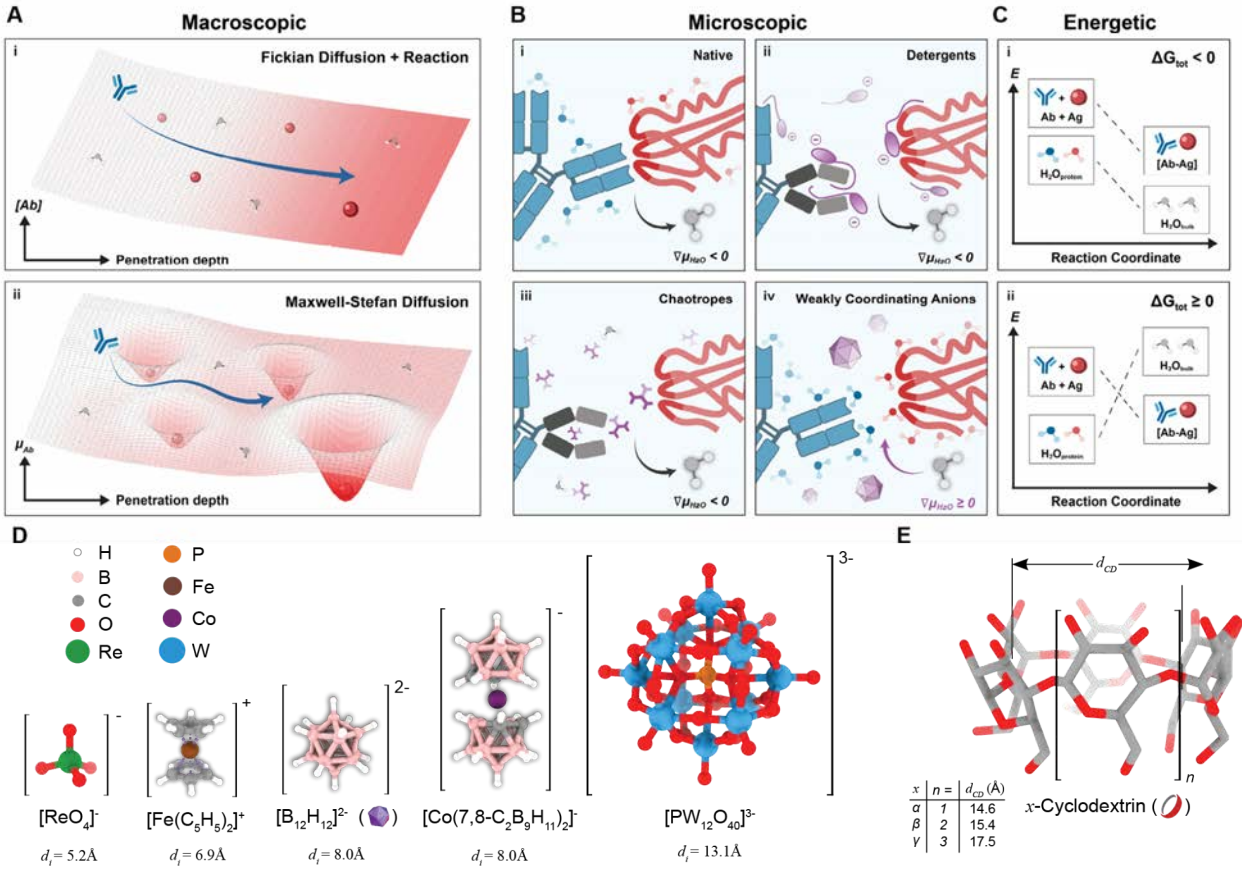

Figure 1. INSIHGT conceptualization and key components. (**A-C**) Reconceptualization of the biomolecular transport and binding phenomena. (**A**) Macroscopic view. (***i***) The traditional Fickian reaction-diffusion model, where biomolecular transports are driven by their respective concentration gradients, and reactions occur locally. (***ii***) The proposed Maxwell-Stefan diffusion model, where biomolecular transports are driven by chemical potential gradients coupled with intermolecular friction, and reactions occur in modifiable potential wells. (**B**) Microscopic view. (***i***) Native antibody-antigen binding (in an aqueous medium) requires the desolvation of their solvation shells ($\nabla\mu_{H2O} < 0$). (***ii, iii***) Detergents and chaotropes solubilize proteins by masking binding sites (and displacing the solvent shell), but they may lead to protein denaturation in high concentrations (black arm of the antibody). (***iv***) Weakly coordinating superchaotropes (WCS, e.g., $[B_{12}H_{12}]^{2-}$) instead solubilizes proteins by favoring solvent-protein interactions ($\nabla\mu_{H2O} \geq 0$), striking a balance between protein solubilization and stabilization. (**C**) Energetic view. Antibody-antigen binding (***i***) without WCS, occurs spontaneously with $\Delta G_{tot} < 0$, while (***ii***) with WCA, is unfavourable with $\Delta G_{tot} \geq 0$. (**D**) Structures and ionic diameters (d_i) of weakly coordinating ions tested. (**E**) General structure of cyclodextrins and their cavity opening diameter (d_{CD}).

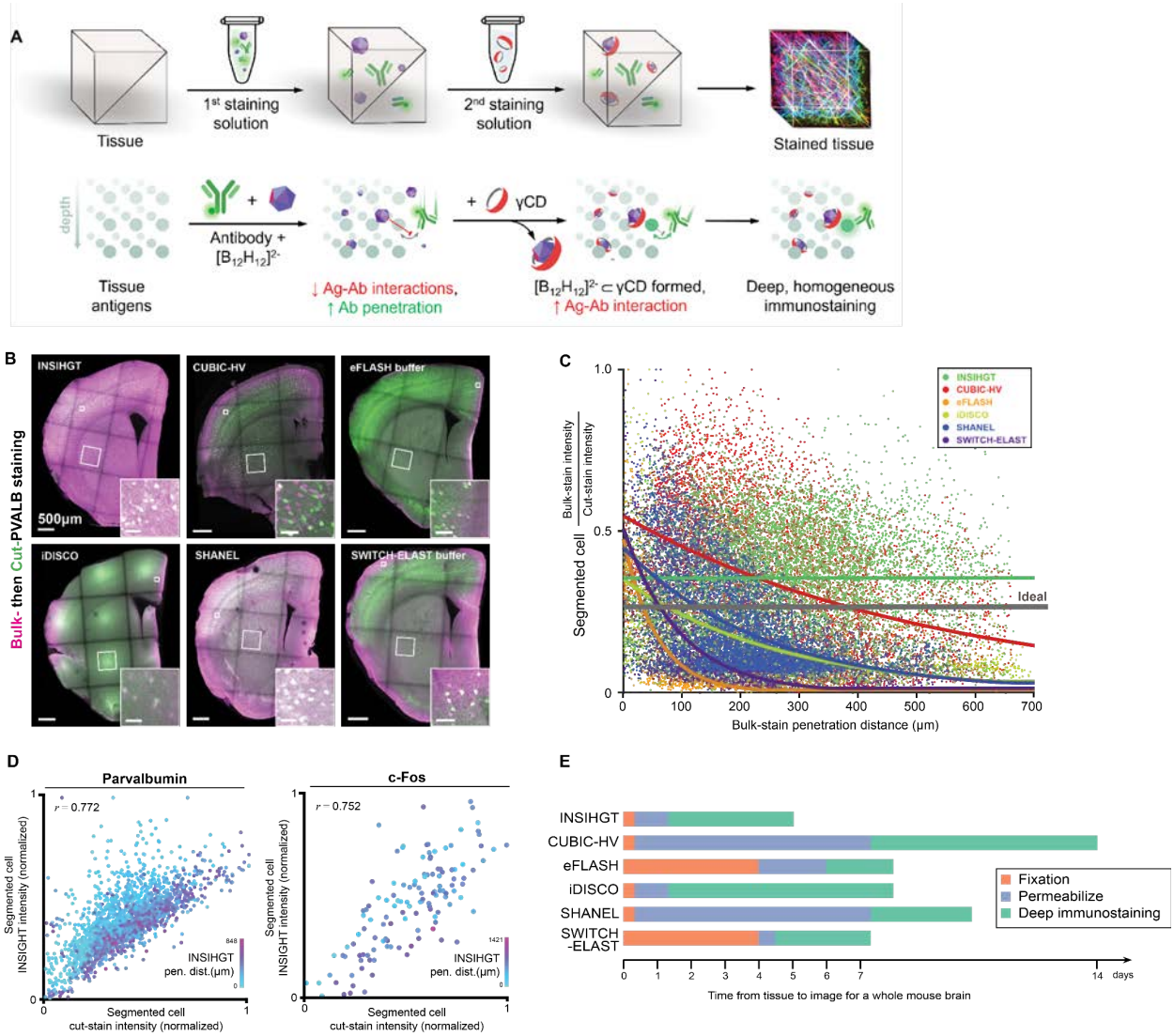

Figure 2. Homogeneous and deep staining with INSIHGT. (**A**) Experimental steps and principle of INSIHGT for immunostaining. Top row: Tissue is infiltrated with antibodies and a weakly coordinating superchoatrope ($[B_{12}H_{12}]^{2-}$, purple dodecahedron) in the 1st staining solution and then transferred into the 2nd solution containing a complexation agent (CD, red ring). Bottom row: The molecular principles of INSIHGT. Weakly coordinating anion prevents antibody-antigen interactions, removing penetration obstacles. After homogeneous infiltration, subsequent γCD infiltration complexes the $[B_{12}H_{12}]^{2-}$ ions, allowing deep tissue immunostaining. (**B**) Benchmark results of six buffers used in deep immunostaining. Enlarged views of smaller areas are shown in insets. Parvalbumin (PVALB) immunostaining signals on cut surface: magenta, bulk-staining signal; green: cut-staining PVALB signal (refer to **Fig. S1**). (**C**) Quantification of bulk:cut-staining signal ratio against penetration distance for segmented cells. Each dot represents a cell. Lines are single-term exponential decay regression curves. The signal decay distance constants (τ) are shown in **Table S1**. Hypothetical ideal method performance is shown as a gray line ($\tau \rightarrow 0+$). (**D**) Correlation of INSIHGT signal with reference (cut-staining intensity) signal, illustrating 3D quantitative immunostaining. r: Pearson correlation coefficient. (**E**) Timeline illustration for a whole mouse brain processing experiment with the different benchmarked methods (drawn to scale, with washing steps omitted).

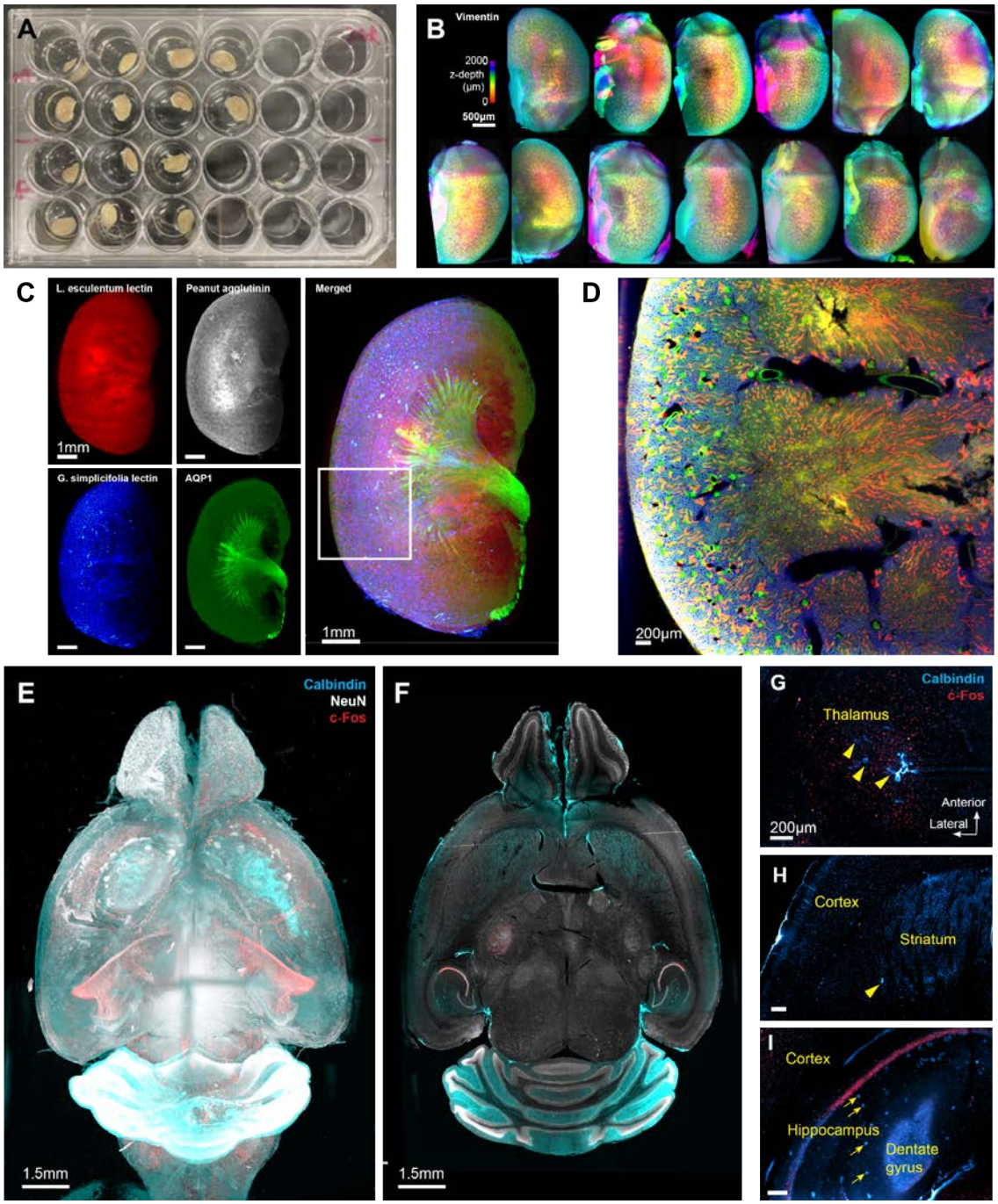

Figure 3. High-throughput whole-organ deep immunostaining with dense mapping using INSIHGT. (**A**) Parallelized sample processing with INSIHGT, exemplified with whole mouse kidneys. (**B**) Whole organ imaging results with parallelized INSIHGT for the samples shown in (**A**), showing vimentin INSIHGT signals color-coded by z-depth. One sample was dropped due to manual errors. (**C-D**) Whole mouse kidney densely multiplexed visualization with *Lycopersicon esculentum* lectin (red), Peanut agglutinin (grey), *Griffonia simplicifolia* lectin I (blue), and AQP-1 (green). (**D**) Enlarged 2D view of the white boxed area in (**C**). (**E-F**) Rendered view of whole mouse brain multiplexed Calbindin, NeuN, and c-Fos mapping of a 3-year-old mouse. (**G-I**) Age-related structural and molecular changes in the thalamus (**G**) and striatum (**H**) with cavitations (indicated by yellow arrowheads), and the hippocampus (**I**) with CALB1-positive deposits (indicated by yellow arrows).

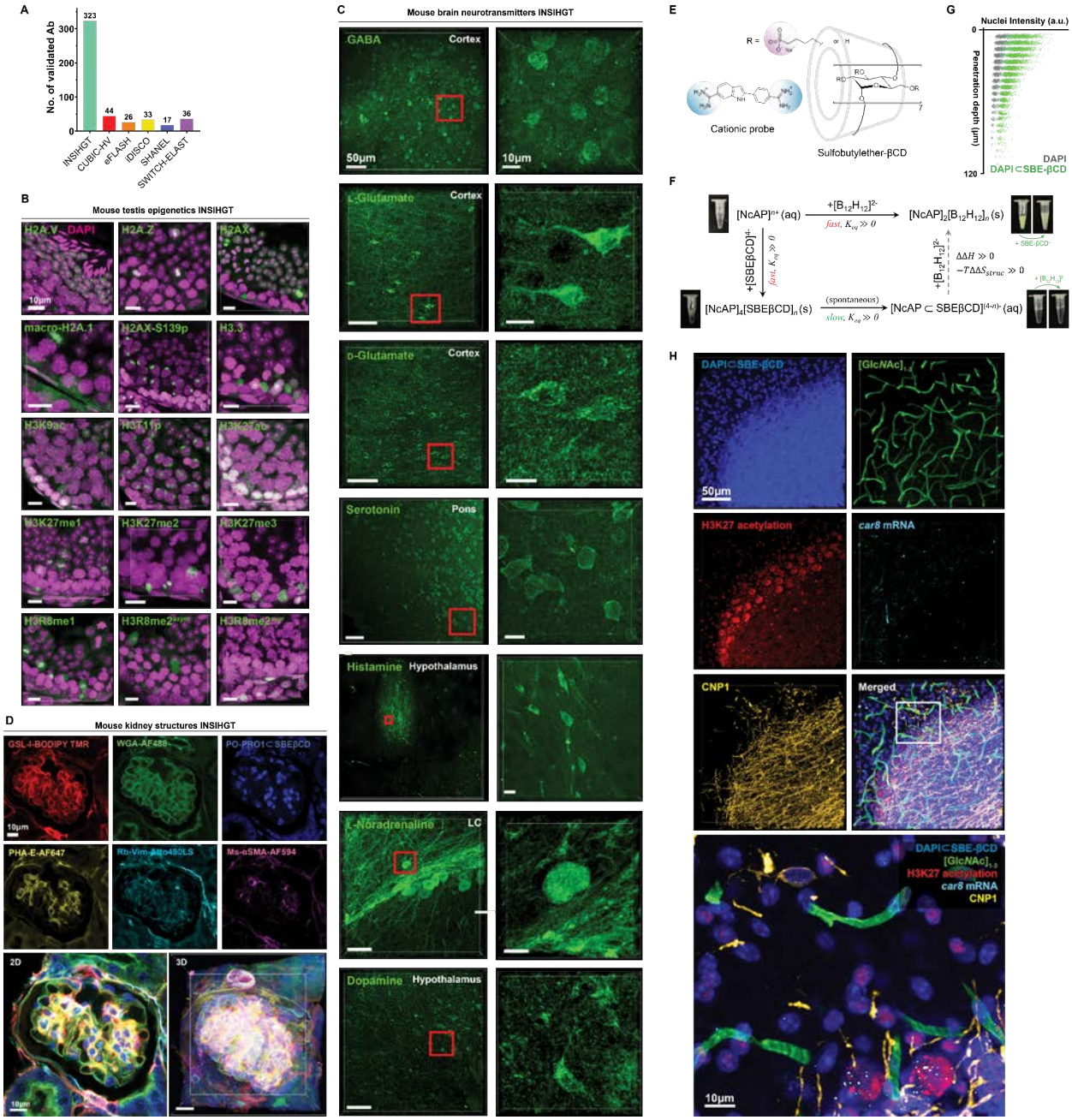

Figure 4. Multi-modality INSIHGT for generality. (**A**) Number of validated antibodies compatible with each benchmarked method. (**B–D**) INSIHGT's compatibility in revealing the 3D location of various features. (**B**) Epigenetic markers based on histone post-translational modifications and isoforms. (**C**) Neurotransmitters. LC: locus ceruleus. (**D**) Structural features, using one-step multiplexed supramolecular histochemistry, multiplexed supramolecular lectin histochemistry, and the supramolecular dye complex [PO-PRO1⊂SBEβCD]. (**E**) Nucleic acid probe (NAP, DAPI structure shown) complexation by SBEβCD for improved tissue penetration. (**F**) Thermodynamic scheme of NAP's complexation reaction with SBEβCD. SBEβCD neither redissolves DAPI/$[B_{12}H_{12}]^{2-}$ precipitates nor precipitates DAPI out from the [DAPI⊂SBEβCD] complex, suggesting kinetic stabilization. (**G**) Quantification of penetration depths of [DAPI⊂SBEβCD] compared to traditional DAPI staining. (**H**) Multimodal 3D molecular phenotyping in a 1mm-thick mouse cerebellum slice for proteins (CNP1), nucleic acids (*car8*, DAPI), epigenetic modifications (H3K27 acetylation), and glycosylations ($[Glc\mathit{N}ac]_{1\text{-}3}$) with INSIHGT. Imaging was limited to 200 μm due to working distance constraints.

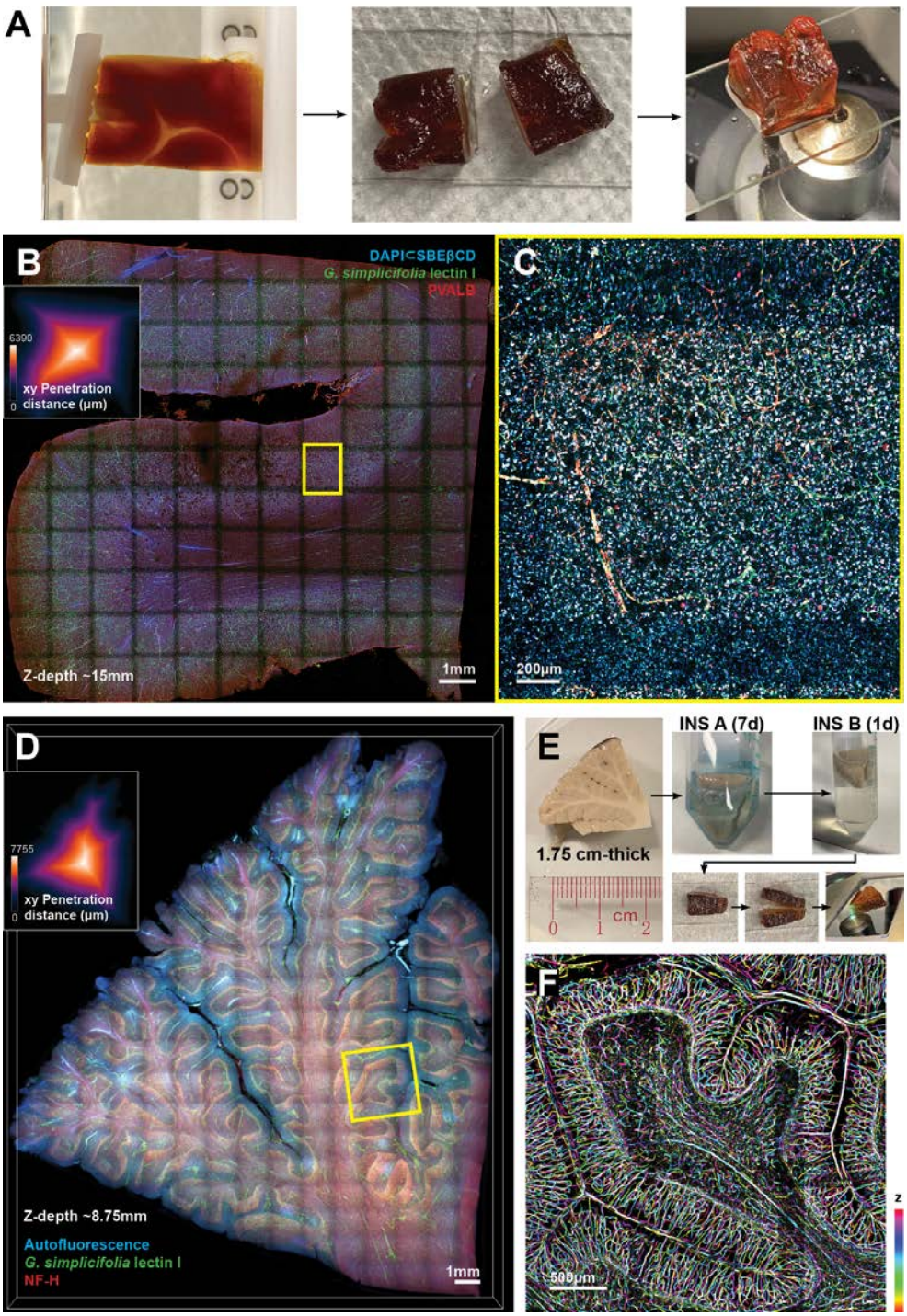

Figure 5. Centimeter-scale INSIHGT for human tissues. (**A**) A human cortex block (1.5 cm × 1.5 cm × 3 cm), processed with INSIHGT and cut in the middle for confocal imaging to confirm penetration depth. (**B**) Confocal tiled image of the cut face from (**A**), stained with [DAPI⊂SBEβCD], *G. simplicifolia* lectin I (GSL-I), and for parvalbumin (PVALB). Inset: penetration depth over the imaging surface. (**C**) Enlarged view of the yellow boxed area in (**B**). (**D**) A human cerebellum tissue block (1.75 cm × 2.0 cm × 2.3 cm) processed with INSIHGT, stained with GSL-I lectin and NF-H. Inset: penetration depth over the imaging surface. (**E**) Illustrated tissue processing steps: tissue is stained for seven days in INSIHGT buffer A (with $[B_{12}H_{12}]^{2-}$), washed in INSIHGT buffer B (with 2HPγCD), and sliced perpendicular to the thinnest dimension at the midpoint. (**F**) Enlarged view of the yellow boxed area in (**D**).

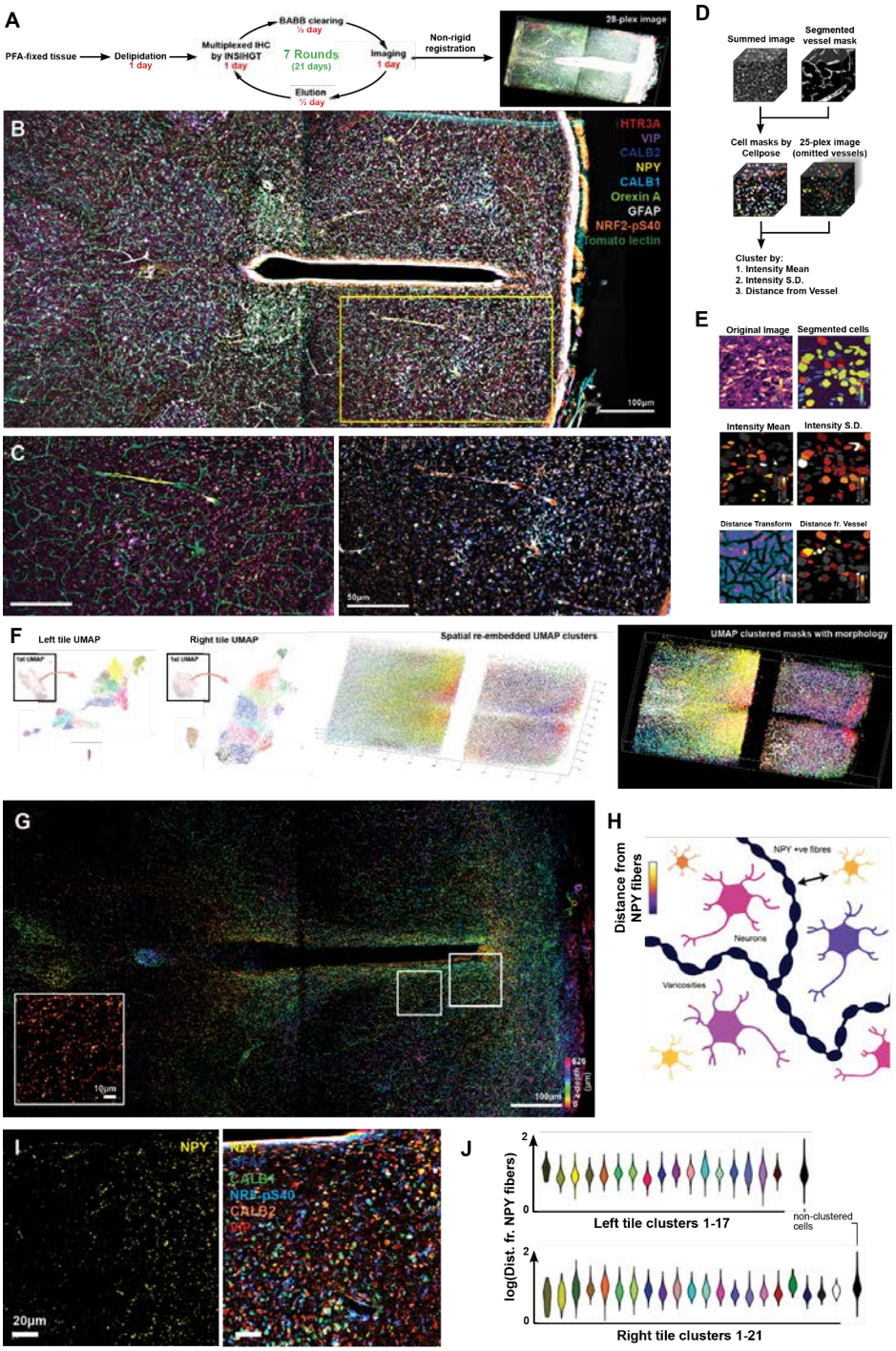

Figure 6. Multi-round multiplexed INSIHGT. (**A**) Schematics of the processing steps for a 1mm-thick mouse hypothalamus sample. (**B**) A selection of multi-round immunostaining signals (for nine targets) displayed for the multi-round multiplexed INSIHGT-processed sample. (**C**) Enlarged view of the yellow boxed area in (**B**) with complementary panel of markers. (**D**) Schematics of the image analysis process. (**E**) Illustrated results of a segmented image subset. The images below show corresponding cell segmentation and quantification results. (**F**) Left panel: Nested UMAP embedding of all segmented cells from both tiles of the image stack. Middle panel: The spatial locations of the different color-coded clusters. Right panel: Similar to the middle panel but with cellular morphology. (**G**) Color-coded *z*-projection of neuropeptide Y (NPY) staining signals. A higher magnification view for the left white boxed area is shown in the inset. (**H**) Schematic representation of distance measurement from NPY fibers to cell bodies via distance transformation. (**I**) NPY signal in a periventricular region (right white boxed area in (**G**)) is shown in the left panel, and with selected markers staining in the right panel. (**J**) Quantification of distance from NPY-expressing fibers for each cell type shown in violin plots, based on the 3D spatial locations of somas and NPY fibers.

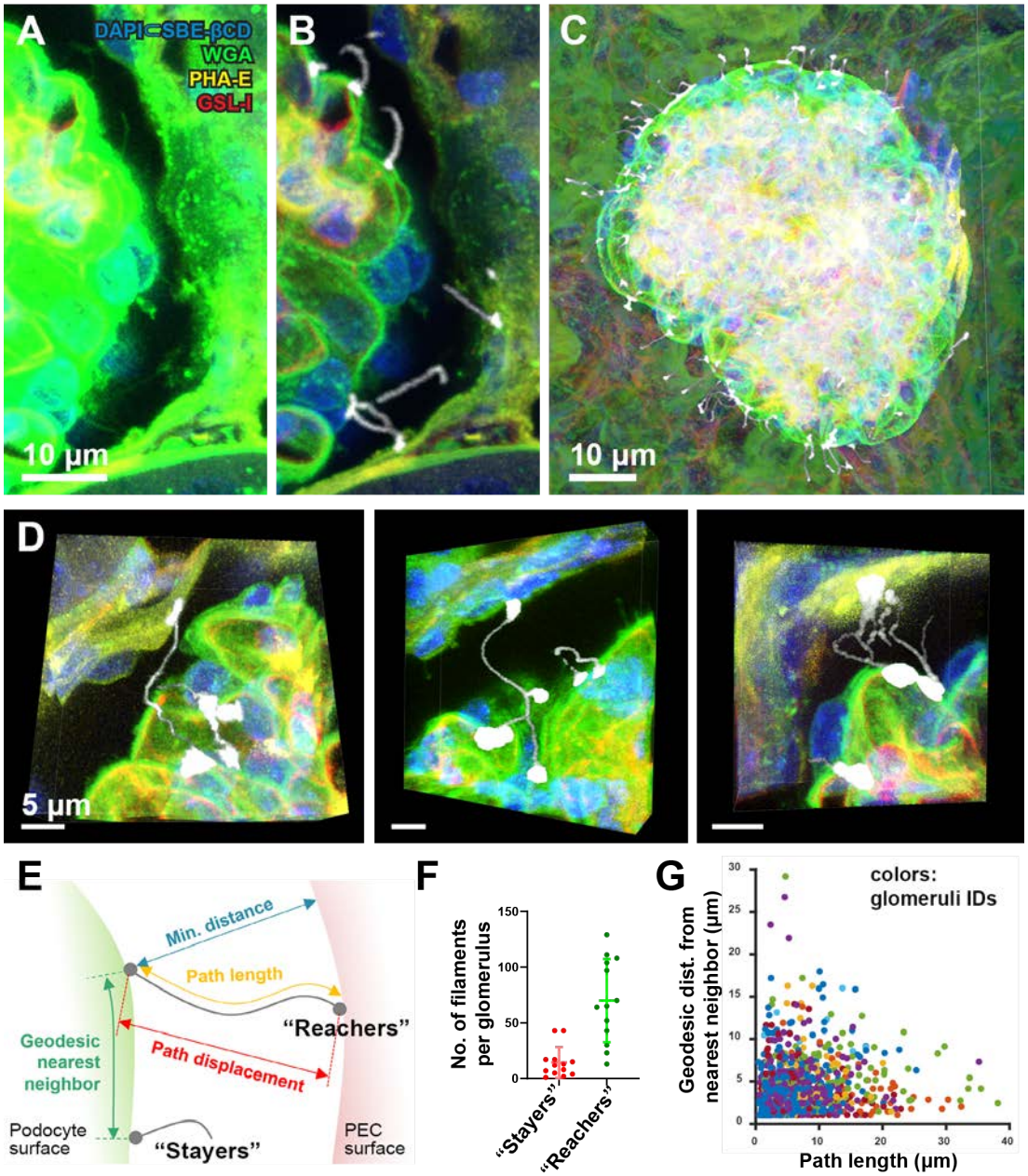

Figure 7. INSIHGT reveals novel intercellular filaments traversing the Bowman space in mouse kidneys. (**A**) Original image of multiplexed image of whole mouse glomerulus with full Bowman capsule. WGA: Wheat germ agglutinin, PHA-E: *Phaseolus vulgaris* hemagglutinin, GSL-I: *Griffonia simplicifolia* lectin I. (**B**) Segmentation of microfilaments with en bloc preservation of native morphologies and spatial relationships in 3D Euclidean space. (**C**) Global representation on the 3D spatial distribution of microfilaments across the entire Bowman space. (**D**) Distinct and protean morphologies of the podocyte-to-parietal epithelial cell (PEC) microfilaments. (**E**) Schematic representation of reachers (contacting PEC surface) and stayers (remaining in the Bowman space) originating from podocyte surfaces with the related physical parameters. (**F**) Descriptive statistics of microfilament subtypes per analyzed glomeruli. N = 14 glomeruli analyzed across 4 mice. (**G**) Correlation between the path length of each microfilament and the geodesic distance between its podocytic attachment point and its nearest neighbor. The data points were color-coded based on their glomerulus of origin in the dataset.

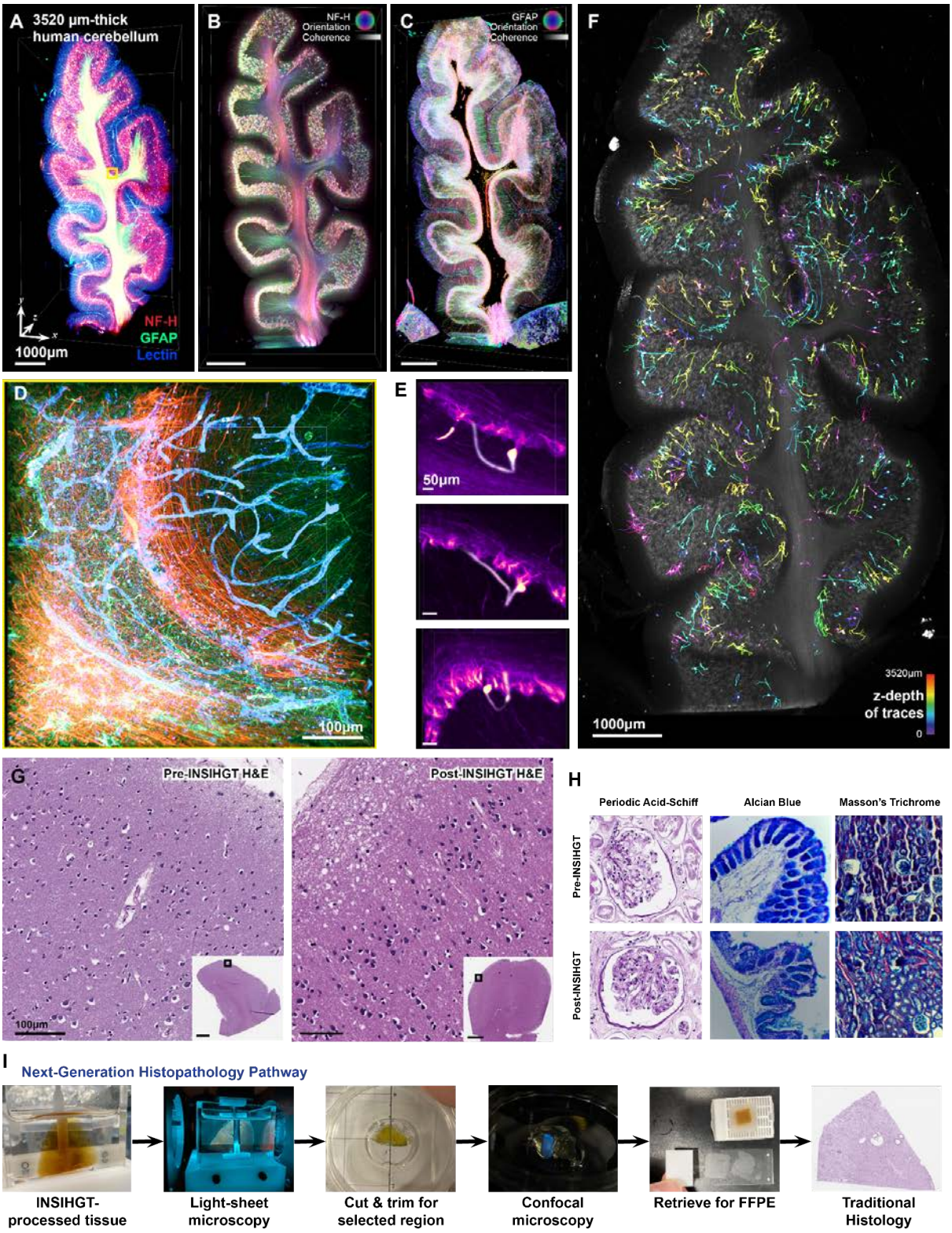

Figure 8. INSIHGT enables non-destructive characterization and analysis of human clinical samples. (**A**) A 3.5mm-thick human cerebellum triplex-stained for glial filaments (GFAP), neurofilament (NF-H) and blood vessels (*G. simplicifolia* lectin I). (**B-C**) Orientation and coherence (or fractional anisotropy) visualization of neurofilament (**B**, NF-H) and glial filament (**C**,

GFAP) via structure tensor analysis. (**D**) Enlarged view of the boxed area in (**A**) via post-hoc confocal microscopy. (**E**) Prototypical morphology of human cerebellar neurofilament inclusions, where their extensions may loop back to the Purkinje layer and occasionally to another inclusion body (lowest image). (**F**) Overview of the 1078 manually traced neurofilament inclusions across the cerebellar sample, color-coded by z-depth. (**G-H**) Traditional 2D histology with special stains on pre-INSIHGT and post-INSIHGT processed samples. (**G**) H&E staining of human brain, (**H**) Left to right: Periodic acid-Schiff (PAS), Alcian blue, and Masson's trichrome staining of human kidney, mouse colon, and mouse kidney sections respectively. (**I**) The Next-Generation Histopathology Pathway. INSIHGT is compatible to traditional histological pipelines, empowering a multi-pronged approach to maximizing the information extracted from clinical samples.

Methods

Materials

Chemicals and reagents

The antibodies utilized in this study are listed in **Table S2**. Secondary Fab fragments or nanobodies were acquired from Jackson ImmunoResearch or Synaptic Systems, and all lectins were sourced from VectorLabs. Conjugation of secondary antibodies and lectins with fluorophores was achieved through *N*-hydroxysuccinimidyl (NHS) chemistry. The process was conducted at room temperature for a duration exceeding 16 hours, using a ten-fold molar excess of the reactive dye-NHS ester. Dodecahydro-*closo*-dodecaborate salts and other boron cluster compounds were procured from Katchem, while cyclodextrin derivatives were obtained from Cyclolab, Cyclodextrin Shop, or Sigma Aldrich.

Human and animal tissues

All experimental procedures were approved by the Animal Research Ethics Committee of the Chinese University of Hong Kong (CUHK) and were performed in accordance with the Guide for the Care and Use of Laboratory Animals. Adult male C57BL/6 were utilized. These mice were housed in a controlled environment (22-23°C) with a 12-hour light-dark cycle, provided by the Laboratory Animal Service Center of CUHK. Unrestricted access to a standard mouse diet and water was ensured, and the environment was maintained at <70% relative humidity. Tissues were perfusion formaldehyde-fixed and collected by post-mortem dissection. In the case of immunostaining for neurotransmitters where Immusmol antibodies were used, the tissues were perfusion-fixed with the STAINperfect™ immunostaining kit A (Immusmol) with the antibody staining steps replaced with those in our INSIHGT method.

For human tissues, brain and kidney tissues were donated post-mortem by a patient were used in this study. Prior ethics approvals have been obtained and approved by the Institutional Review Board with consent from the donor and his family. Human dissection was performed by an anatomist (HML) after perfusion fixation with 4% paraformaldehyde via the femoral artery. The post-mortem delay to fixation and tissue harvesting was 4 weeks at -18°C refrigeration.

Methods

Benchmarking experiments

We designed a stringent benchmarking scheme for quantitative evaluation of antibody penetration depth and signal homogeneity across depth for comparison across existing deep immunostaining methods, based on our previously described principles (**Fig S1A**) [2]. The benchmarking experiment is carried out in two parts, the first part using a whole mouse hemisphere stained in bulk with anti-Parvalbumin (PV) antibodies with excess AlexaFluor 647-conjugated secondary Fab fragments - termed bulk-staining - after which the tissue is cut coronally at defined locations using a brain matrix and re-stained with anti-PV antibodies and AlexaFluor 488-conjugated secondary Fab fragments - termed cut-staining (**Fig S1A**). Hence,

signals from bulk-staining can be distinguished easily from cut-staining and reveal different penetration depths of the two-staged immunostaining. We tested different deep immunostaining methods in the bulk-staining stage of the experiments, while the cut-staining was performed in 1× PBS with 0.1% Tween-20 as a conventional immunostaining buffer.

All benchmarking samples were perfusion-fixed with 4% paraformaldehyde (PFA) in 1× PBS followed by post-fixation in 4% PFA overnight at 4°C, except for SHIELD and SWITCH-ELAST samples where the SHIELD protocol was used. In addition, the final RI matching where the benzyl alcohol/benzyl benzoate (BABB) clearing method was universally employed to standardize the changes in tissue volumes and hence penetration distance adjustments. For bulk-staining during our benchmarking experiment, we followed the published protocols except for eFLASH and SWITCH-ELAST due to the lack of specialized in-house equipment.

For eFLASH [11], we stained the SHIELDed and sodium dodecyl sulphate (SDS) delipidated tissue in the alkaline sodium deoxycholate buffer (240mM Tris, 160mM CAPS, 20% w/v D-sorbitol, 0.9% w/v sodium deoxycholate) and titrated-in acid-adjusting booster buffer (20% w/v D-sorbitol and 60mM boric acid) hourly over 24 hours to achieve a -0.1 ± 0.1 pH/hr adjustment rate. The tissue was then washed with 1× PBSTN (1× PBS, 1% v/v Triton X-100 and 0.02% w/v NaN_3) 2 times 3 hours each before imaging.

For SWITCH-ELAST [3,12,14], we stained the SHIELDed and SDS-delipidated tissue with the antibody and Fab fragments in 0.2×PBSNaCh (0.2× PBS, 5% w/v NaCh and 0.02% w/v NaN_3, 5% v/v normal donkey serum) first for 1 day at 37°C without embedding the SHIELDed tissue in elastic gel nor compression/stretching, followed by adding Triton X-100 to a final concentration of ~5% and incubated for 1 more day. The tissue was then washed with 1× PBSTN 2 times 3 hours each before imaging.

For CUBIC HistoVision [4] and iDISCO [15], the tissue was processed and stained as previously described [5].

For SHANEL [16], the tissue was first delipidated with CHAPS/NMDEA solution (10% w/v CHAPS detergent and 25% w/v *N*-methyldiethanolamine in water) for 1 week, then further delipidated with dichloromethane/methanol as in iDISCO, then treated with 0.5M acetic acid for 2 days, washed in water for 6 hours repeated 2 times, and then treated with guanidinium solution (PBS with 4M guanidinium chloride, 0.05 sodium acetate, 2% w/v Triton X-100) for 2 days, blocked in blocking buffer (1× PBS, 0.2% v/v Triton X-100, 10% v/v DMSO, 10% goat serum) for 1 day, and finally stained in antibody incubation buffer (1× PBS, 0.2% v/v Tween-20, 3% v/v DMSO, 3% v/v goat serum, 10 mg/L heparin sodium) for 1 week.

For quantification, PV-positive cells were identified using a Laplacian of Gaussian (LoG) filter, followed by intensity-based segmentation. These segmented masks allow the quantification of bulk- and cut-staining channel intensities, in addition to the distance transformation intensity, performed in MATLAB R2023a (MathWorks, US). For an ideal deep

immunostaining, the bulk-immunostaining signals should be independent of the bulk-staining penetration distances computed with distance transform of the segmented tissue boundaries, and perfectly correlate with that of cut-immunostaining. This is often not the case, as "rimming" of bulk-staining signals inevitably occurs as a "shell" around the tissue due to more easily accessible antigens on the bulk-staining tissue surface (**Fig. S1B**). The rimming effect can be quantified by fitting a single-term exponential decay curve

$$\frac{\text{bulk-staining intensity}}{\text{cut-staining intensity}} = e^{-\tau(\text{bulk-staining penetration distance})}$$

and evaluating the decay constant, tau (τ), across penetration depths, with $\tau \rightarrow 0^+$ as we approach the ideal case.

Screening chemicals for INSIHGT

We first pre-screened the weakly coordinating anions by immunostaining for parvalbumin in $1mm^3$ of mouse cortex tissue cubes in the presence of 0.1M weakly coordinating superchaotropes, after 1 day of incubation at room temperature the staining solution was aspirated and 0.1M corresponding cyclodextrin was added and incubated overnight. The tissue was then washed in PBSN for 15 minutes 2 times and cleared with the benzyl alcohol/benzyl benzoate (BABB) method, and imaged. This procedure eliminated $[B_{12}Br_{12}]^{2-}$, $[B_{12}I_{12}]^{2-}$, and $[PW_{12}O_{40}]^{3-}$ (as cesium or sodium salts) as they do not give the correct immunostaining pattern or lead to tissue destruction. We tested $[Fe(C_5H_5)_2]^+$ (as the hexafluorophosphate salt) for the sake of completion as a low-charge large-sized cation.

To benchmark the ability in achieving deep and homogeneous immunostaining, the above benchmarking procedure was used. Mouse hemibrains were fixed, washed and stained with 1ug rabbit anti-parvalbumin antibody with 1µg AlexaFluor 647-labeled donkey anti-rabbit secondary antibody Fab fragments in 0.1M of the weakly coordinating anions. The staining proceeded for 1 day after which the solution was replaced with 0.1M corresponding cyclodextrin (or its derivatives) and incubated overnight. The hemibrains were then washed in PBSN for 1 hour 2 times, cut in the middle coronally and re-stained for parvalbumin using AlexaFluor 488-labeled secondary Fab fragments. The tissue was then washed, cleared with the BABB method, and imaged on the cut face using a confocal microscope.

INSIHGT

A detailed step-by-step protocol used in this study has been given below. As a general overview, tissues were typically fixed using formalin or 4% paraformaldehyde, thoroughly washed in PBSN, and pre-incubated overnight at 37°C in INSIHGT buffer A. The tissues were then stained with a solution containing the desired antibodies, Fab fragments, lectins, and SBEβCD-complexed nucleic acid probes in INSIHGT buffer A, ensuring a final $[B_{12}H_{12}]^{2-}$ concentration of 0.25 M. Staining duration varied from 6 hours to 10 days based on tissue size, antigen, and required homogeneity (please see the calculation of time *t* in the step-by-step protocol). Post-staining, the solution was aspirated and replaced with INSIHGT buffer B (0.25M

2-hydroxypropyl-γ-cyclodextrin in PBS) without prior washing, followed by a minimum 6-hour incubation with adequate shaking of the viscous buffer. After sufficient PBSN washing, tissues were ready for imaging or clearing. Over incubation for any steps up to 60 days was tolerable. After imaging, the antibodies can be eluted with 0.1M sodium sulphite in INSIHGT buffer A at 37°C overnight.

Screening antibodies compatible with INSIHGT

We compiled a list of antibodies, reviewed their tissue expression and staining patterns in the literature, then obtained the respective ~1mm^3 tissues. After performing INSIHGT and BABB clearing using 96-well plates, we imaged the tissues and assessed the staining specificity. The total fixed tissue-to-image time for the antibody compatibility test is < 36 hours.

Comparison between 2D histological staining of post-INSIHGT and control tissues

Mouse and human samples were pre-processed as described above. Tissues were divided into the post-INSIGHT treated group which underwent the INSIHGT protocol with 3 days of INSIHGT A incubation without the application of antibodies and 6 hours of INSIHGT B incubation, plus BABB clearing, and the control group which was immersed in PBSN for an equivalent period of time. Both groups were immersed in 70% ethanol, preceded by the immersion in 100% ethanol for the post-INSIHGT group (which were in BABB), and in 50% ethanol for the control group (which were in PBSN). Tissues were then immersed in 100% ethanol, xylene, and paraffin as in the standard paraffin embedding process. The embedded tissues were cut into 5 µm (human) or 10 µm (mouse) sections followed 2D histological staining with special stains. Following standard protocols, H&E staining was performed on human brain and kidney, PAS staining was performed on human kidney, Alcian blue staining was performed on mouse colon, and Masson trichrome staining was performed on mouse kidney samples.

Microscopy

Microscopic imaging was performed with either a Leica SP8 confocal microscope, or a custom-built MesoSPIM v5.1 [17].

Quantification and data analysis

Image processing

No penetration-related attenuation intensity adjustments were performed for all displayed images except for 3D renderings in **Fig. 3C, E, F** to provide the best visualization of internal signal. We employed an intensity transformation mask based on the exponent of the distance from the whole organ mask surface. Image segmentation was performed with Cellpose 2.0 [13] for cells implemented in MATLAB R2023b or Python, or with simple intensity thresholding. Affine and non-linear image registration was performed in MATLAB R2023a or manually in Adobe After Effects 2020 using the mesh warp effect and time remapping for *z*-plane adjustment. Image stitching was performed either with ImageJ BigStitcher plugin [18] or assisted manually with Adobe After Effects 2020 followed by tile allocation using custom written scripts in MATLAB R2023a.

3D image visualization and Movie rendering were performed with Bitplane Imaris 9.1, which were done as raw data with brightness and contrast adjustments.

Segmentation and analysis of podocyte-to-PEC microfilaments in mouse kidneys

Podocyte-to-PEC microfilaments of 14 mouse kidneys were manually traced via the SNT plugin in ImageJ [19]. Path properties of the tracings were then exported for further analysis using custom codes in MATLAB R2023a. Distance transforms were performed under manually curated glomerulus and bowman space masks, such that each voxel value corresponds to the distance between that voxel and the nearest nonzero voxel of the Bowman space mask. Path displacement d_{fil} was computed via Pythagoras theorem using the start and end coordinates of the filament . Minimal distance d_{min} is defined as the voxel value difference between the start and end coordinates. Path length d_{path} is directly measured via SNT. Tortuosity is defined as $d_{path/}\ d_{fil}$, skewness is defined as $d_{fil/}\ d_{min}$, and the angle of take-off is defined as the angle between the unit gradient vector of the distance transform and the unit path displacement vector. The geodesic distance $d_A(p,q)$ between voxels $p,q \in A$ is defined as the minimal of length L of path(s) $P = (p_1, p_2, \ldots, p_l)$ connecting p,q, where A is the set of all voxels constituting the surface of the glomerular mask [20]:

$$d_A(p,q) = \min\{L(P) : p_1 = p, p_l = q, P \subseteq A\}$$

Correlation statistics were then performed via GraphPad Prism version 8 for Windows, GraphPad Software, Boston, Massachusetts USA, www.graphpad.com. Tracing and statistical analysis for the human cerebellar neurofilament inclusions were performed analogously.

Spatial orientation and fractional anisotropy visualization of human cerebellum neural and glial filaments

To visualize cerebellar neural and glial fibers in their preferred orientations, we performed structure tensor analysis with orientation-based color-coding in 3D.

In detail, let $G : \mathbb{R}^3 \times \mathbb{R}_+ \to \mathbb{R}$ be a 3D Gaussian kernel with standard deviation σ:

$$G(x, y, z, \sigma) = \frac{1}{(2\pi\sigma^2)^{\frac{3}{2}}} \exp\left(-\frac{x^2 + y^2 + z^2}{2\sigma^2}\right).$$

Define a 3D image as a function $I : \mathbb{R}^3 \to \mathbb{R}$ which outputs the spatial voxel values. The gradient $\nabla I : \mathbb{R}^3 \to \mathbb{R}^3$ of I at each voxel is obtained by convolving I with the spatial derivatives of G:

$$\nabla G(x, y, z, \sigma) = \left(\frac{\partial G}{\partial x}, \frac{\partial G}{\partial y}, \frac{\partial G}{\partial z}\right),$$

$$\nabla I = I * \nabla G,$$

where $*$ denotes the convolution operation.

Compute the structure tensor $T : \mathbb{R}^3 \to \mathbb{R}^{3\times 3}$ as the outer product of ∇I with itself:

$$T(x, y, z) \quad = \nabla I \otimes \nabla I$$

T is then smoothed over a neighbourhood N via convolution with G to give $\bar{T}$:

$$\begin{aligned} \bar{T}(x, y, z) \quad &= G * T(x, y, z) \\ &= \begin{bmatrix} \langle I_x^2 \rangle_N & \langle I_x I_y \rangle_N & \langle I_x I_z \rangle_N \\ \langle I_y I_x \rangle_N & \langle I_y^2 \rangle_N & \langle I_y I_z \rangle_N \\ \langle I_z I_x \rangle_N & \langle I_z I_y \rangle_N & \langle I_z^2 \rangle_N \end{bmatrix}, \end{aligned}$$

where $\langle \cdot \rangle_N$ represents the Gaussian-weighted smoothing over N [21,22].

Eigendecomposition of $\bar{T}$ is then performed to define the shape (eigenvalues, λ) and the orientation (eigenvectors, v_e) of the diffusion ellipsoid. The fractional anisotropy (FA) is then computed from λ:

$$FA = \sqrt{\frac{(\lambda_1 - \lambda_2)^2 + (\lambda_2 - \lambda_3)^2 + (\lambda_3 - \lambda_1)^2}{2(\lambda_1^2 + \lambda_2^2 + \lambda_3^2)}}.$$

where FA ranges from 0 (complete isotropic diffusion) to 1 (complete anisotropic diffusion) [23].

The tertiary (least) eigenvalue-associated eigenvectors were then extracted for the 3-dimensional image volume, with the 4th dimension encoding the corresponding vector basis magnitudes. To visualize the orientation of fibers in the context of the image, the eigenvectors were intensity-modulated with both the fractional anisotropy and the original image voxel values, and represented as a 3D RGB stack for visualization in Imaris.

Multi-round multiplexed 3D image processing and analysis

As the images were acquired across multiple rounds on a confocal microscope, we encountered the issues of misalignment and z-step glitching due to piezoelectric motor errors. Hence, the tiles of images can neither be directly stitched nor registered across multiple rounds. A custom MATLAB code was written to manually remove all the z-step glitching, followed by matching the z-steps across multiple rounds aiding by using the time-remapping function in Adobe After Effects, with linear interpolation for the transformed z-substacks. The resulting glitch-removed, z-matched tiles were then rigid registered using the image registration application in MATLAB, followed by non-rigid registration for local matching. Finally the registrated tiles were stitched for downstream processing.

Before segmentation, all non-vessel channels underwent background subtraction. They were then summed to capture the full morphology of stained cells, followed by segmentation using Cellpose 2.0 [13]. Vessels were segmented based on their staining intensity, and a distance transform was used to obtain the distance from vessels for all voxels. The cell masks subsequently facilitated the acquisition of the statistics for all stained channels.

UMAP was performed in MATLAB R2023a using the UMAP 4.4 [18,24] package in a nested manner, incorporating the means and standard deviations of all immunostaining intensities, as well as the distance to the nearest blood vessel. An initial UMAP was applied to each image stack tile, followed by DBSCAN clustering to eliminate the largest cluster based on cell count. The remaining cells were subjected to a second UMAP, where another round of DBSCAN clustering yielded the final cell clusters for analysis.

Violin plots for each clustered cell type's distance from neuropeptide Y-positive fibers were obtained by creating a distance transformation field from the segmented fibers. Segmented cell masks were used to compute the mean intensity value of the distance transformation field. The pairwise distances of the clustered cell types were obtained for the 30 nearest neighbors, followed by calculating the mean and SD for the coefficient of variation. The gramm package in MATLAB R2023a was used for plotting some of the graphs [25]

INSIHGT Protocol

This protocol describes the INSIHGT process for staining fixed or permeabilized tissues.

Materials

PBSN (1× PBS with 0.02% w/v NaN_3)	Sodium dodecahydrododecaborate ($Na_2B_{12}H_{12}$)
Methanol	2-hydroxypropyl-γ-cyclodextrin (2HPγCD)
Dichloromethane	Nucleic acid probe (optional)
Sodium sulphite (Na_2SO_3, optional)	Sulfobutylether-β-cyclodextrin (SBEβCD, optional)

Buffers/Solutions

INSIHGT buffer A (2×): 0.5M $Na_2B_{12}H_{12}$ in PBSN

INSIHGT buffer B (1×): 0.25M 2HPγCD in PBSN

INSIHGT buffer C (1×): 0.25M SBEβCD in PBSN

Procedure overview

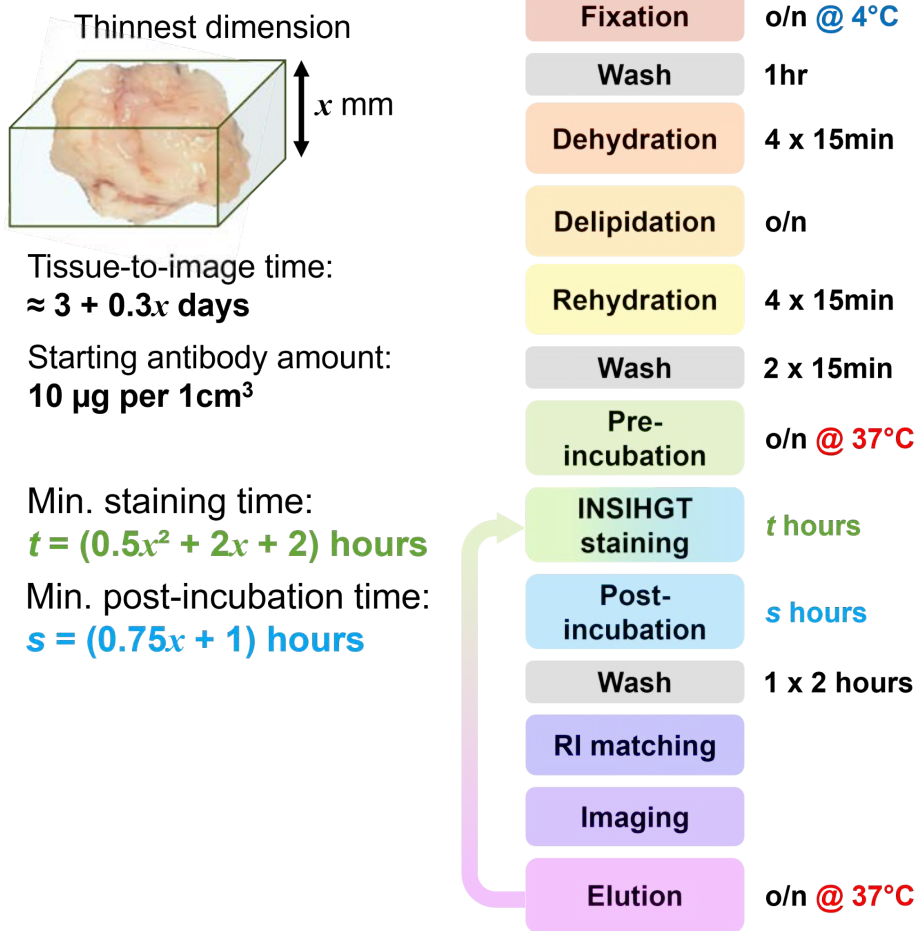

Procedure

The procedure below is illustrated for a 1 cm^3 tissue sample but can be scaled as needed.

0. **Fixation:** Fix tissue overnight at 4°C with formaldehyde, glutaraldehyde or SHIELD-fixation. Wash in 5 ml PBSN for 1 hour at room temperature (r.t.) with shaking.

1. **Dehydrate** by shaking incubation in 5 ml 50% v/v methanol/water, then 5 ml 100% methanol repeated 3 times, 15 min with shaking at r.t. for each step.

2. **Delipidate** by shaking incubation in 5 ml 2:1 v/v mixture of dichloromethane/methanol overnight at r.t. Use a glass or polypropylene containers (e.g. microcentrifuge tubes), in a well-ventilated hood with adequate shaking.

3. **Rehydration:** Repeat the dehydration steps in reverse order, then 2 × 15 min washes in PBSN.

4. **Pre-Incubation:** Incubate in 2 ml 1× INSIHGT buffer A at 37°C overnight with shaking.

5. **Prepare nucleic acid probe (optional):** Prepare 200 nmol of the probe by mixing it with INSIHGT buffer C in a 1:1 v/v ratio.

6. **INSIHGT Staining:**

a. Place the tissue in a container that fits its size well.

b. Add enough 2× INSIHGT buffer A to around half-cover the tissue.

c. Add the desired amount of primary antibodies (start with 10μg each).

d. Add the prepared nucleic acid probe in INSIHGT buffer C (if desired).

e. Add corresponding fluorophore-labeled secondary antibody Fab fragments or nanobodies (in the same μg amount as the primary antibody used), or lectins if desired.

f. Add PBSN to make the final concentration of INSIHGT buffer A to 1x. The volume required will be equal to the volume added in step 6a - (total volume added in step 6c, 6d, and 6e).

g. Top up with 1x INSIHGT buffer A to just cover the entire tissue.

h. Incubate at r.t. for 3 days (or *t* hours, see below) with shaking. Protect from light.

7. **Post-incubation:** Incubate the stained tissue in 3 ml INSIHGT buffer B at r.t. overnight (or *s* hours, see below) with shaking. Place the tube horizontally to ensure adequate mixing.

8. **Wash**: Wash in 5 ml PBSN three times for 2 hours each at r.t., shaked horizontally.

9. **Refractive index matching** (optional): Example for BABB clearing:

- Repeat the dehydration steps.
- Prepare BABB: 1:2 v/v mix of benzyl alcohol / benzyl benzoate.
- Place tissue in 5ml BABB at r.t. overnight with shaking. Refresh BABB until tissue is clear.

10. **Imaging**: Confocal, light-sheet and two-photon microscopies are all compatible.

11. **Stripping** (optional): Strip tissue in 2 ml 1× INSIHGT buffer A + 0.1 M Na_2SO_3 at 37°C overnight with shaking. Wash twice with 2 ml 1× INSIHGT buffer at 37°C for 2 hours each.

12. **Repeat staining** (optional): Proceed to step 6 for the next round of staining.

Notes

- All incubation periods can be extended up to one month without harm.
- Tissues delipidated with methods other than CH_2Cl_2/Methanol are acceptable, except if the buffer contains Triton X-100 or triethylamine. Tween-20 is compatible.
- Test pretreatment buffer compatibility with INSIHGT. Mix 100µl of the buffer with 2× INSIHGT buffer A in a 1:1 ratio. If precipitation occurs, test each buffer component individually and exclude any that cause precipitation from your modified buffer.
- Avoid contact between 100% dichloromethane and plastics (except with polypropylene or PTFE tips or Eppendorf tubes). It dissolves plastics and makes the solution cloudy.
- The minimum staining time (t hours) in step 8 depends on the thinnest dimension (x, in mm) of the tissue. Calculate t as $0.5x^2 + 2x + 2$.
- The minimum post-incubation time (s hours) in step 9 is $s = 0.75x + 1$.
- If staining is uniform, staining time can be reduced. Conversely, if penetration is inhomogeneous, extend the staining time by 1.5×. There is no need to adjust post-staining incubation and washing.
- Increasing antibody concentration in the staining solution by 1.5× can also enhance penetration homogeneity. Conversely, if staining is uniform and signal-to-noise is satisfactory, antibody concentration can be reduced.
- If using fluorophore-labeled whole IgG secondary antibodies or streptavidins, perform steps 6–8 with primary antibodies only, then repeat for secondary antibodies starting from step 4. There is no need to post-fix primary antibodies.
- To visualize endogenous fluorescence, staining them with anti-fluroescent protein antibodies is the best solution. Alternatively, one can attempt ethyl cinnamate (ECi) [26,27] with triethanolamine replacing triethylamine as pH adjusting agent, or dibenzyl ether clearing after tetrahydrofuran (THF) dehydration [28]. SHIELD-based protection with aqueous-based refractive index matching can also be used after omitting Triton X-100 in all the buffers.
- After staining, the sample can be stored in PBSN at 4°C or in BABB at r.t. indefinitely.

Graphical summary of INSIHGT protocol

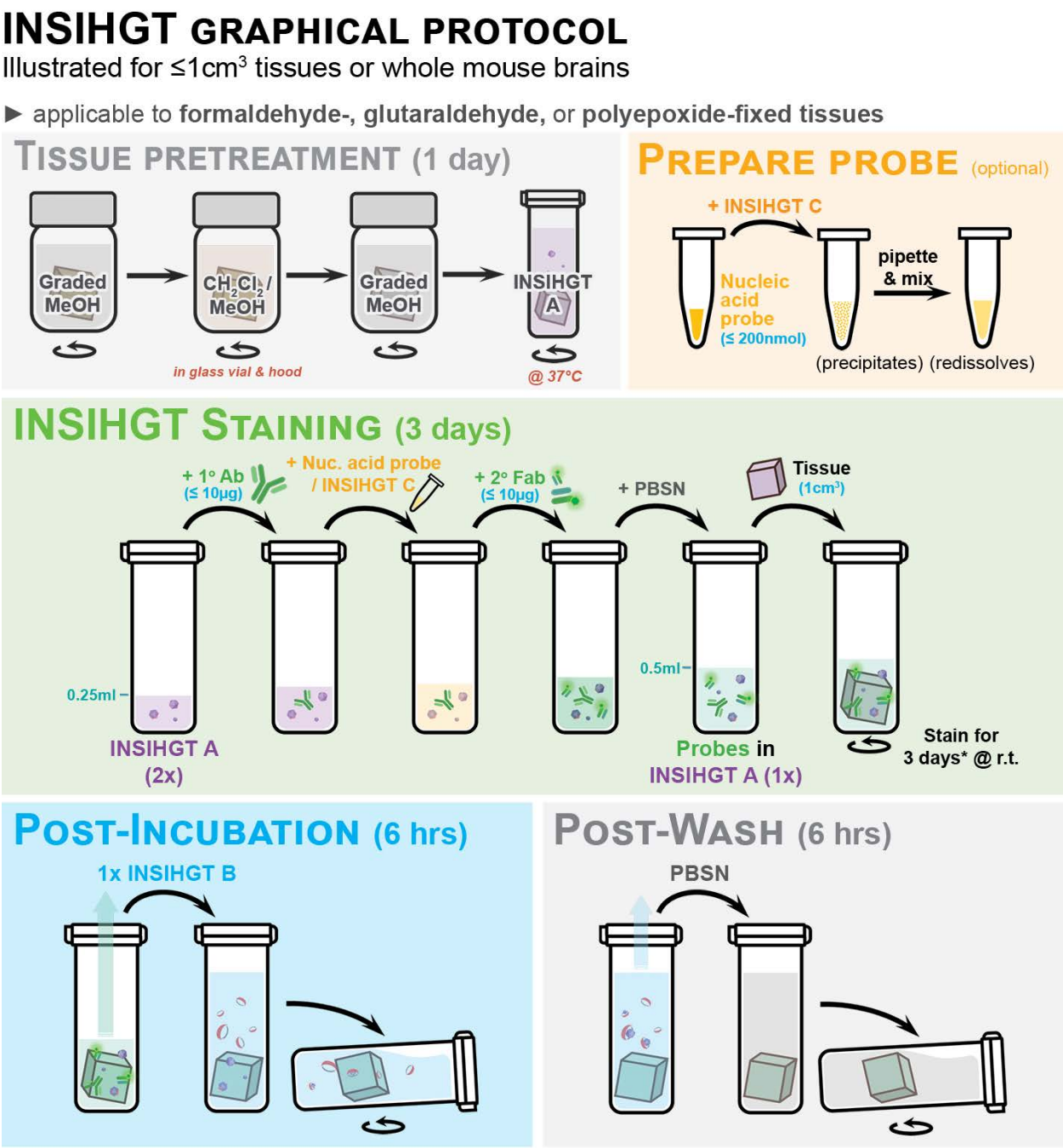

** Can reduce the staining time or amount of antibodies used if penetration homogenetiy is ideal; conversely, increase the staining time, or antibody concentration, or both if it is not.*

Supplementary Text

Summary of theoretical formulation

Here we provide a brief overview of our updated theoretical formulation on the reaction-diffusion processes involved in 3D histochemistry.

1. Macroscopic scale

Thermodynamic states are defined by observable macroscopic parameters in equilibrium. In our case where only binding reactions were involved, the numbers of molecules are conserved. Hence, the **Gibbs free energy** constitutes the usable work that is not stored within covalent bonds, which is always in decline as they are dissipated through an increase in entropy, providing the fundamental drive on the system's evolution.

When probes are introduced locally into a tissue populated with targets, they diffuse down their chemical potential gradients until a dynamic equilibrium is reached. In a multi-component system, the fluxes of chemical species are interdependent, which is aptly described by the **Maxwell-Stefan diffusion**. With no formation of new molecular species in a binding reaction, we can quantify the reaction extent by the proximity of probes to targets, rather than the concentration of reactants and products as in the traditional reaction-diffusion model. The closer the probes are to the targets, the lower the system's Gibbs energy, and the greater the reaction extent. This essentially converts a binding reaction to a multicomponent diffusion process via Gibbs free energy.

2. Microscopic scale

Macroscale thermodynamic parameters emerge from the microscopic arrangements of molecules averaged over time and different matching ensembles, which are quantitatively captured with statistical mechanics. At equilibrium, the **Kirkwood-Buff Integral** provides the preferential solvation of one species around another in a multicomponent system, providing a picture of how molecules will be arranged when the multicomponent system reaches its lowest energy state. It links how probes will stay proximal or distal from their target based on their statistical preference around other species in the environment. **Kirkwood-Buff Integral Inversion** can thus provide the molecular arrangements given a set of thermodynamic parameters, which can be experimentally measured.

3. Fine temporal scale

While the statistical average captures an overview of the molecular picture, the time scales of each molecular arrangement dictate how much they will contribute to the averaged overview. Stochastic models, such as the **Fokker-Planck equation**, provide a stochastic perspective on the kinetics of intermolecular interactions. The **Smoluchowski equation** models the damped mechanics of these molecular collisions, which also considers the presence of force fields that can drive a preferred direction of movement. In the case of potential wells in binding reactions, the probe naturally diffuses and drifts through the energy landscape in a multicomponent mixture, as described in the **Kramers-Eyring formula**. If an agent is introduced to flatten this

energy landscape, i.e., reduce the energy differences between e.g., the bound and unbound states, it can lead to more frequent probe entry and escape of the target's potential well.

4. Dynamical evolution

All the above theories, from macroscale to microscale, only hold in near-equilibria conditions. Which trajectory the system will evolve from its initial state to its final state is still an open question, Specifically, it has been proposed under certain conditions (which are satisfied by the Smoluchowski equation) that globally, the system will evolve along a path with a minimized entropy production - the so-called **Minimum Entropy Production Principle**. However, locally such a principle will not hold. How a local subsystem is defined which recapitulates the global system evolution trajectory remains an open question in thermodynamics.

In summary, by reconceptualizing reaction-diffusion as multicomponent diffusion, we can model probes and other constitutive species as diffusing down their chemical potential gradients both macroscopically (diffusion) and microscopically (reaction), where they solubilize in the environment with the lowest free energies. Reshaping such energy landscapes through the use of solubilizing agents and in situ chemical reactions can then control the motion of probes selectively.

Weakly coordinating superchaotropes as non-denaturing protein solubilizers

For proteins, the significant role of intramolecular interactions in intermolecular interactions complicates the picture. Ideally, intermolecular interactions were selectively disturbed for solubilization, with minimal disturbance on intramolecular interactions to prevent denaturation. We reasoned that if the interactions between the native solvent (i.e., water) and proteins are promoted, the intramolecular forces (e.g., hydrophobic interactions) of proteins that evolved in an aqueous environment will help maintain their current folded state. This contrasts with agents that have significant affinities towards the proteins, which may compete against the intramolecular forces and disrupt their folding, such as with detergents [29] and strong hydrogen-bonding agents like urea [30]. Hence, an ideal protein solubilizer is water soluble yet poorly coordinating with both water and proteins. The ideal weakly-coordinating superchaotropes have low charge-to-volume ratios and lack hydrophobic groups to avoid affinities towards protein hydrophobic surfaces. We thus screened the literature for counter anions used in the isolation of extremely electrophilic species for crystallography [31] or as conjugate bases of superacids, which includes perchlorate, perrhenate, and dodecaborates.

Physicochemical properties of closo-dodecahydrododecaborate

The *closo*-dodecahydrododecaborate $[B_{12}H_{12}]^{2-}$ was discovered in the 1950s and stands out as a remarkably stable member of boron cluster compounds and boron hydrides. It can withstand sustained dry heating, strong acids and alkalis, and diverse reactive organic or inorganic chemicals. Its chemical inertness has been attributed to the 3D aromaticity of the ion - a Hückel's rule generalization in planar aromatic compounds. Apart from chemical inertness,

$[B_{12}H_{12}]^{2-}$ is also poorly coordinating, exemplified by the super-acidic character of its Brønsted acid $H_2B_{12}H_{12}$ (pK_a = 28) [32] and perhaps by the stabilization of the conjugate base by delocalizing the two electrons over a large surface area. The combined weak ionic and poorly coordinating properties lead to easy solubilization of the $[B_{12}H_{12}]^{2-}$ ion in diverse solvents, lending the proposal for it to be used for nuclear waste treatment by extracting charged ions into water-immiscible organic solvents. The chemical and coordinative inertness of $[B_{12}H_{12}]^{2-}$ is also directly related to its biological inertness, with an oral lethal dose (LD_{50}) for rats at > 7,500 mg/kg. Hence, the proposed biological applications for $[B_{12}H_{12}]^{2-}$ and its ^{10}B isotopic derivatives were largely related to boron neutron capture therapy (BNCT) *in vivo*. The utility of $[B_{12}H_{12}]^{2-}$ *in vitro* has been scarcely explored. The available solution characteristics of $[B_{12}H_{12}]^{2-}$ is summarized in **Table S4**.

closo-Dodecahydrododecaborate hydration characteristics

Table S4. Basic physical chemistry characteristics of $[B_{12}H_{12}]^{2-}$ [33,34]

Ion radius	400 pm
$T\Delta S_{struct,water}$	14.8 kcal mol^{-1}
ΔHB	-2.31
ΔG_{hyd}	-140 kcal mol^{-1}
ΔH_{hyd}	-145
$T\Delta S_{hyd}$	-5 kcal mol^{-1}
Polarizability	25.7 Å^3 (calculated)
Hydration Δr	9.6 pm (calculated)
Average number of H_2O molecules in hydration shell	1.8 (calculated)
$\Delta_{hyd}S$	-17.9 cal K^{-1} mol^{-1}
K_a with αCD in water	100 L mol^{-1}
K_a with βCD in water	200 L mol^{-1}
K_a with γCD in water	2,000 L mol^{-1}

Interactions of $[B_{12}H_{12}]^{2-}$ with other molecular species

The pair correlation function of $[B_{12}H_{12}]^{2-}$ ion in water has been obtained by simulation. It showed concentric rings of water molecules on top of the hydrogen atoms, with an average

number of water molecules forming ≈10 bridging O–H···H–B dihydrogen bonds (DHB) [35], with a simulated DHB length of 1.76 Å [36] with an estimated bond strength of 7.15 kcal mol^{-1} [37] (*ca.* O–H···O hydrogen bond length in water: 1.97 Å, bond strength 5.0 kcal mol^{-1}). Simulated translational diffusion coefficients of the $[B_{12}H_{12}]^{2-}$ ion in water is $(1.8 \pm 0.2) \times 10^{-9}$ m^2 s^{-1}.

Apart from forming DHBs, $[B_{12}H_{12}]^{2-}$ do have some coordinating activity as per evidence obtained in crystalline solid state [38] and has been shown to interact with adenine directly in aqueous solutions. [34]

Interestingly, at concentrations up to 1.5mM, $[B_{12}H_{12}]^{2-}$ does not disrupt the structure of bovine serum albumin (BSA) at all in 0.1M $NaHCO_3$, does not show any significant interactions with BSA or affect the hydrodynamic radii of BSA even at near 1,000-fold molar excess. It also did not affect the thermal denaturing behavior of BSA. [39]

Supplementary Figures

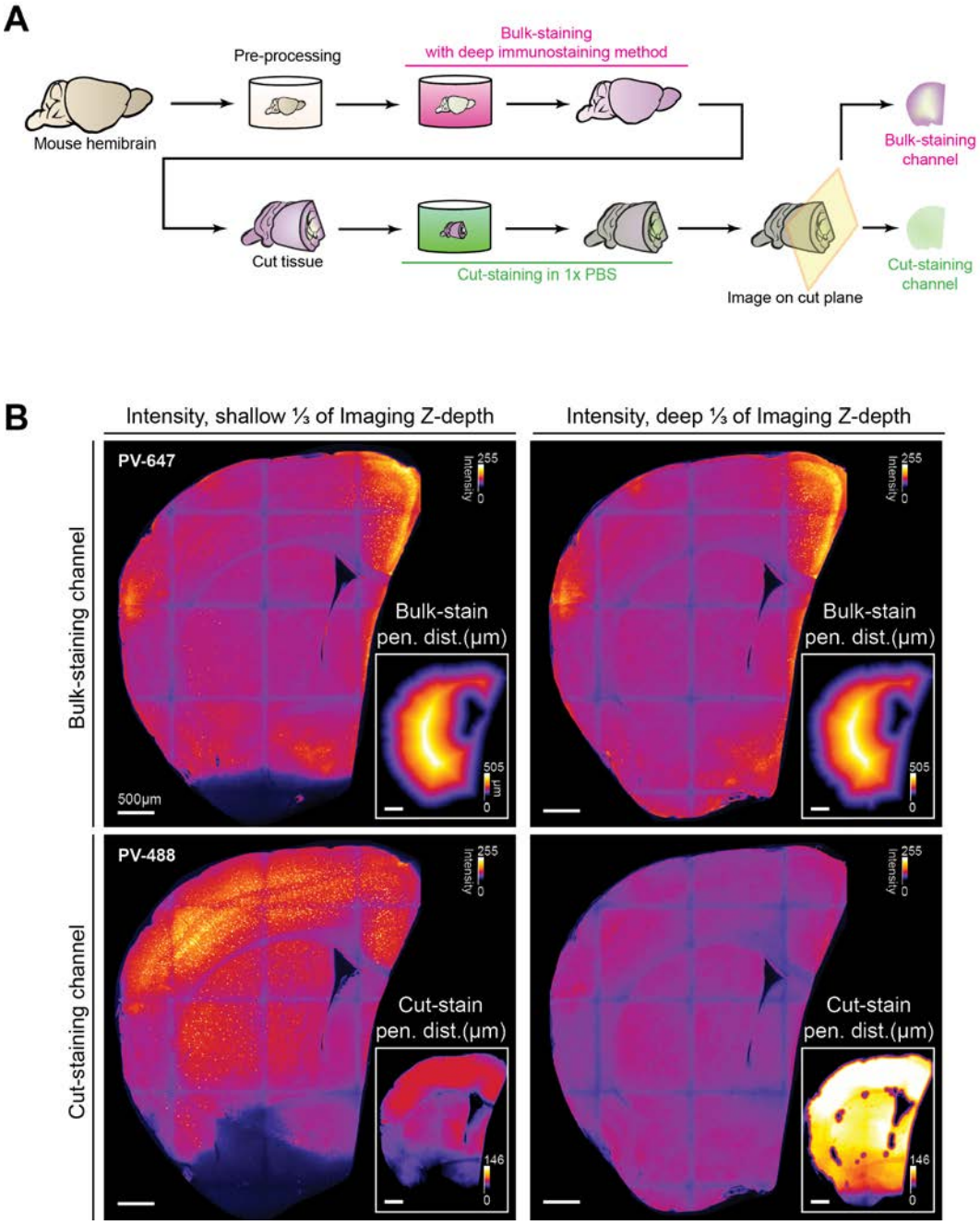

Figure S1. Benchmarking Experiment Design and Principle Illustration. (**A**) The experimental design utilized in this study for stringent benchmarking of antibody penetration depth and homogeneity. (**B**) Typical imaging results from a sample in the benchmarking experiment. The bulk-staining was conducted before tissue cutting, so the bulk-staining intensities (upper row) and their corresponding calculated penetration lengths (insets of upper row) are relatively invariant at the same *z*-depth of imaging (arranged in columns). Conversely, cut-staining was performed after tissue cutting, and antibodies could penetrate through the cut surface, which corresponds to the imaging plane, displayed in the *xy*-plane here (lower row). The penetration distance was irregular and inhomogeneous due to minor tissue curvatures and irregular tissue texture, and areas of lower penetration distances due to vasculatures. These factors were taken into account during the quantification of cut-staining penetration depth (insets of lower row).

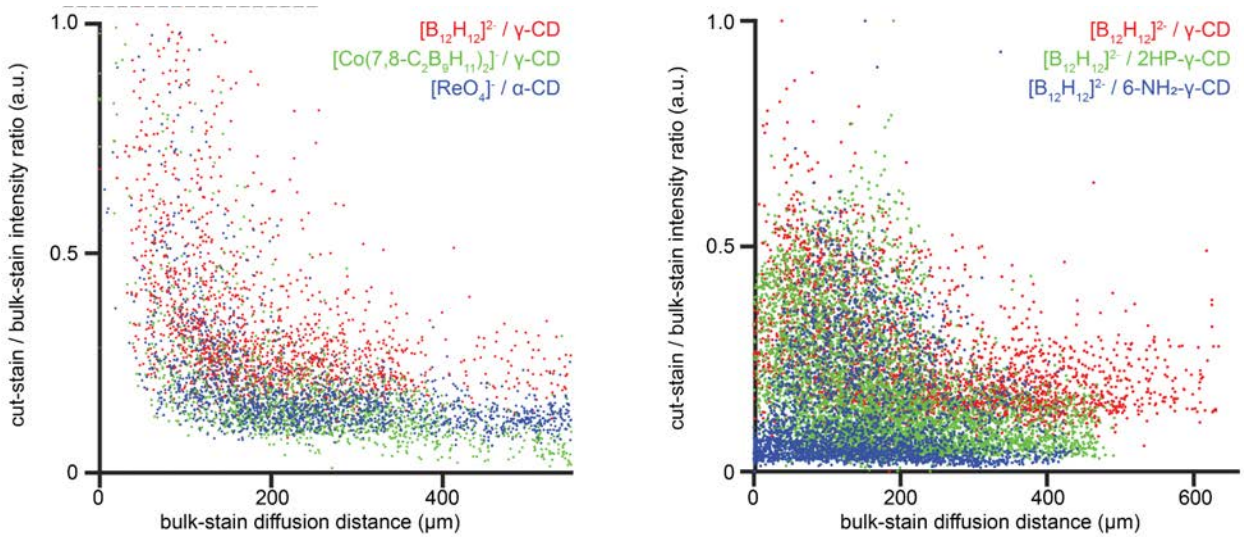

Figure S2. Evaluation of different weakly coordinating anions (left panel) and γ-cyclodextrin derivatives (right panel) using the benchmarking experimental pipeline described in **Figure S1**.

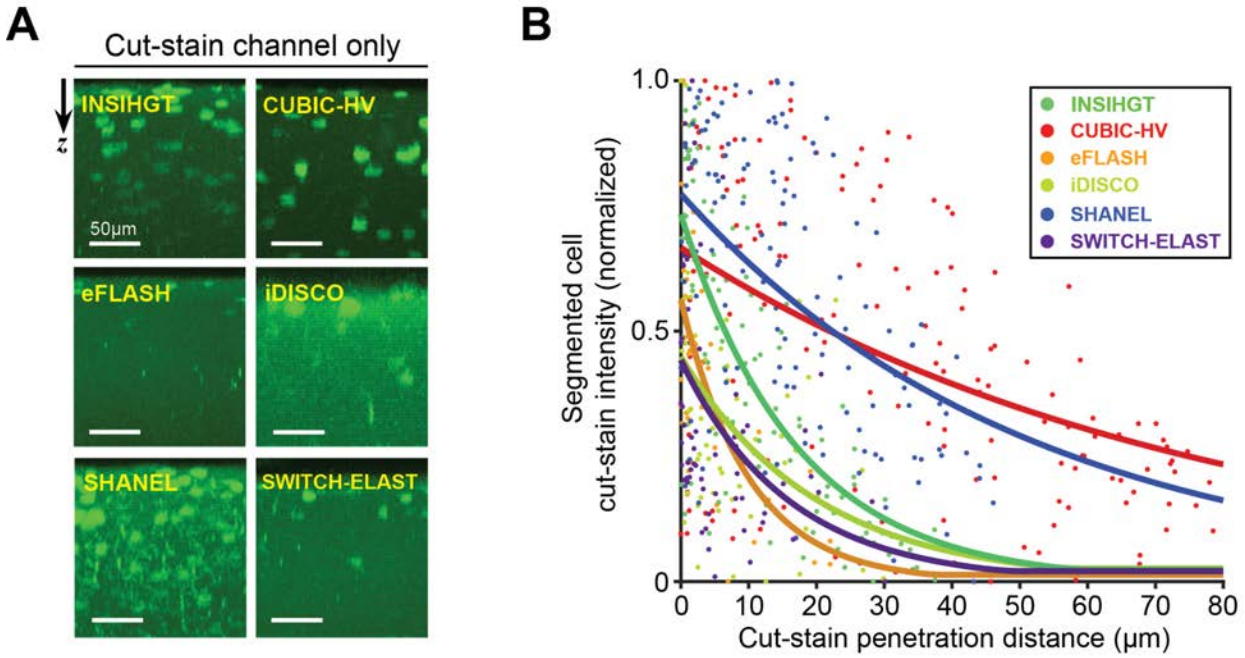

Figure S3. (**A**) *x-z* projection of larger white boxed areas from **Figure 2A** at deep bulk-staining penetration depths, with only the cut-staining channels (without the use of any deep immunostaining methods) shown. The deeper the penetration, the more permeabilized the tissue. (**B**) Quantitative comparison of tissue permeabilization by correlating cut-staining penetration depth and cut-staining intensity.

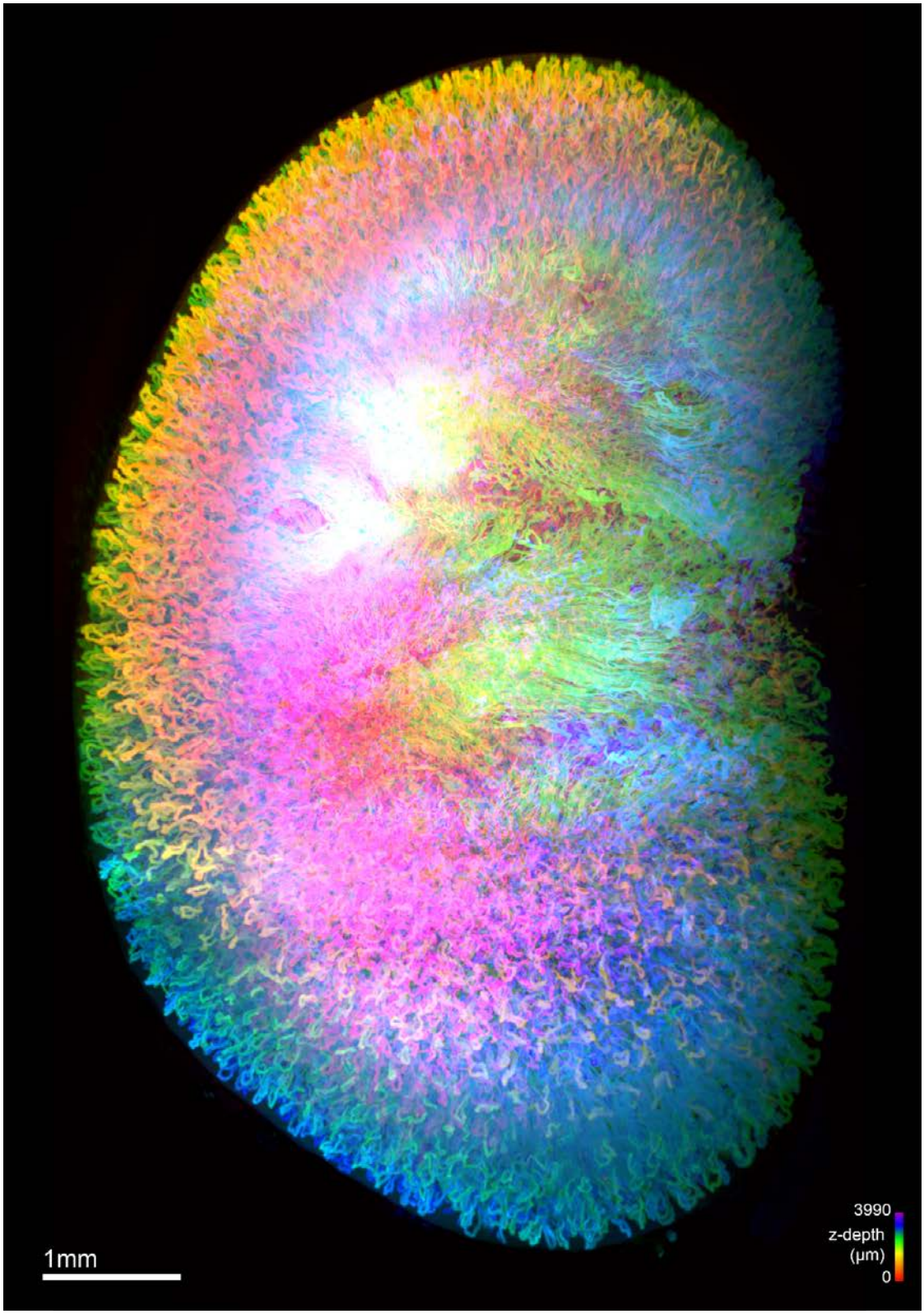

Figure S4. Whole mouse kidney stained with Lycopersicon esculentum (Tomato) Lectin. 3D rendering, colour-coding: z-depth.

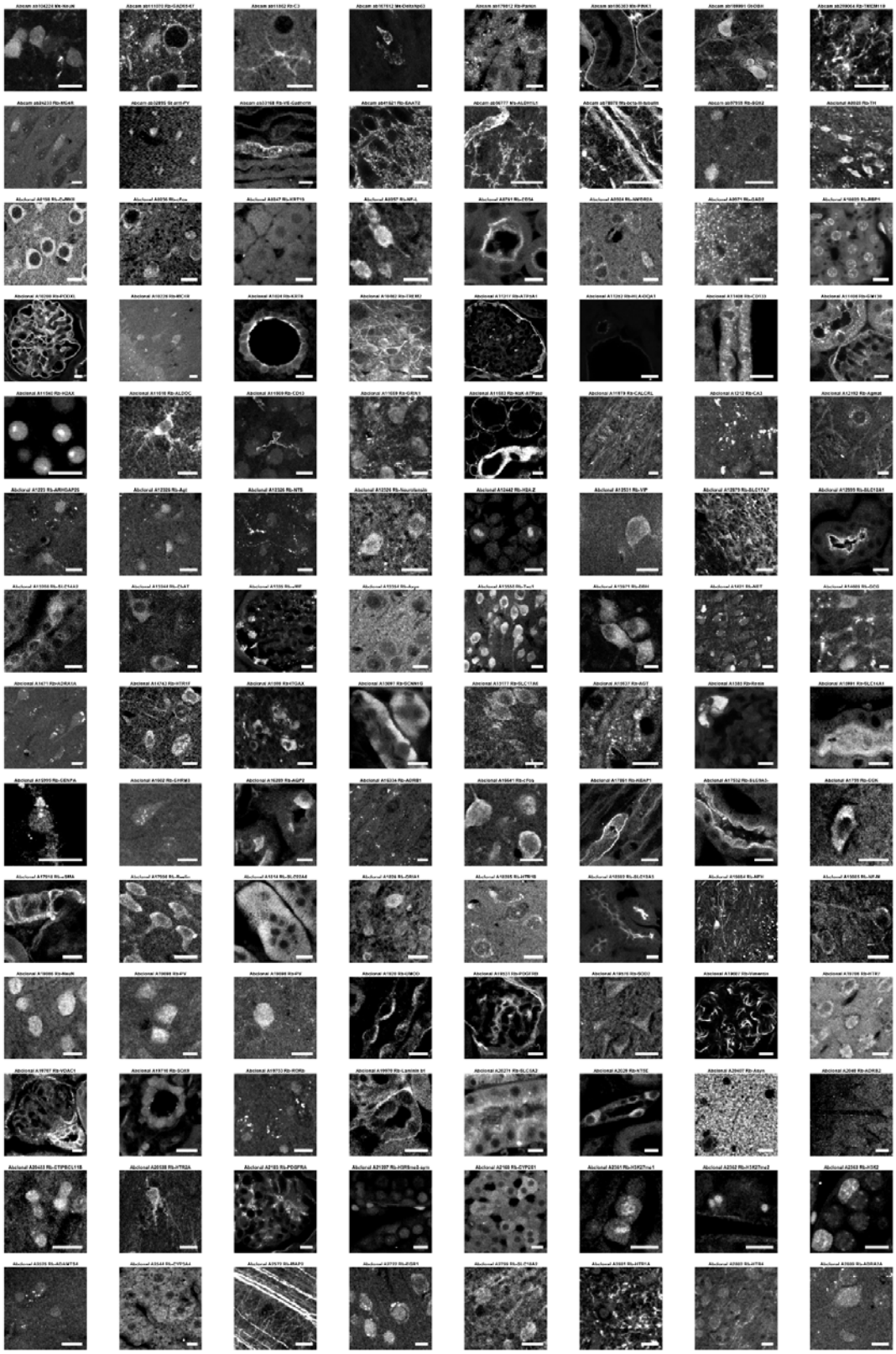

Figure S5. Representative images from INSIHGT-compatible antibodies, Part 1. Scale bars are set to 10 µm.

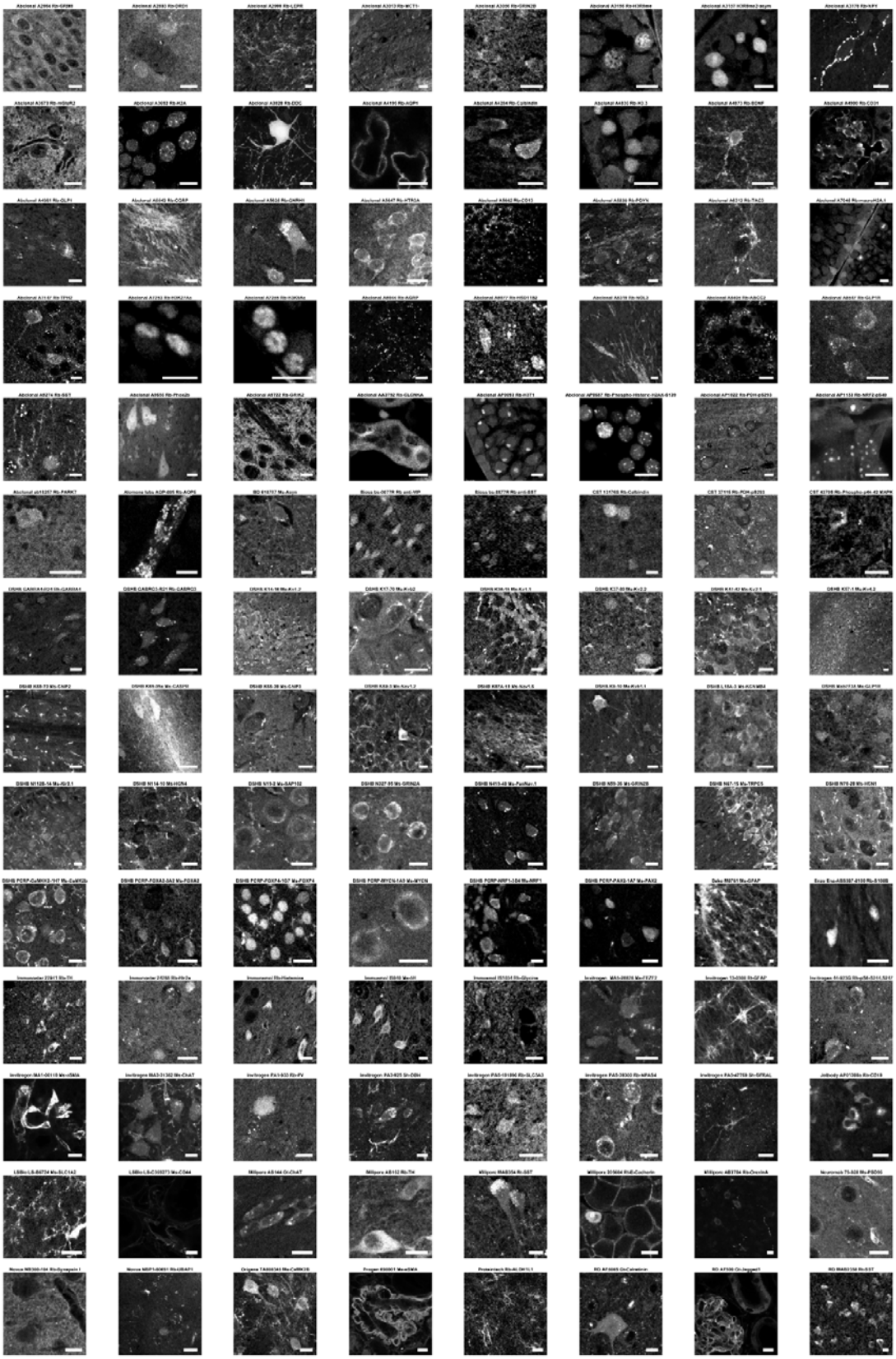

Figure S6. Representative images from INSIHGT-compatible antibodies, Part 2. Scale bars are set to 10 µm.

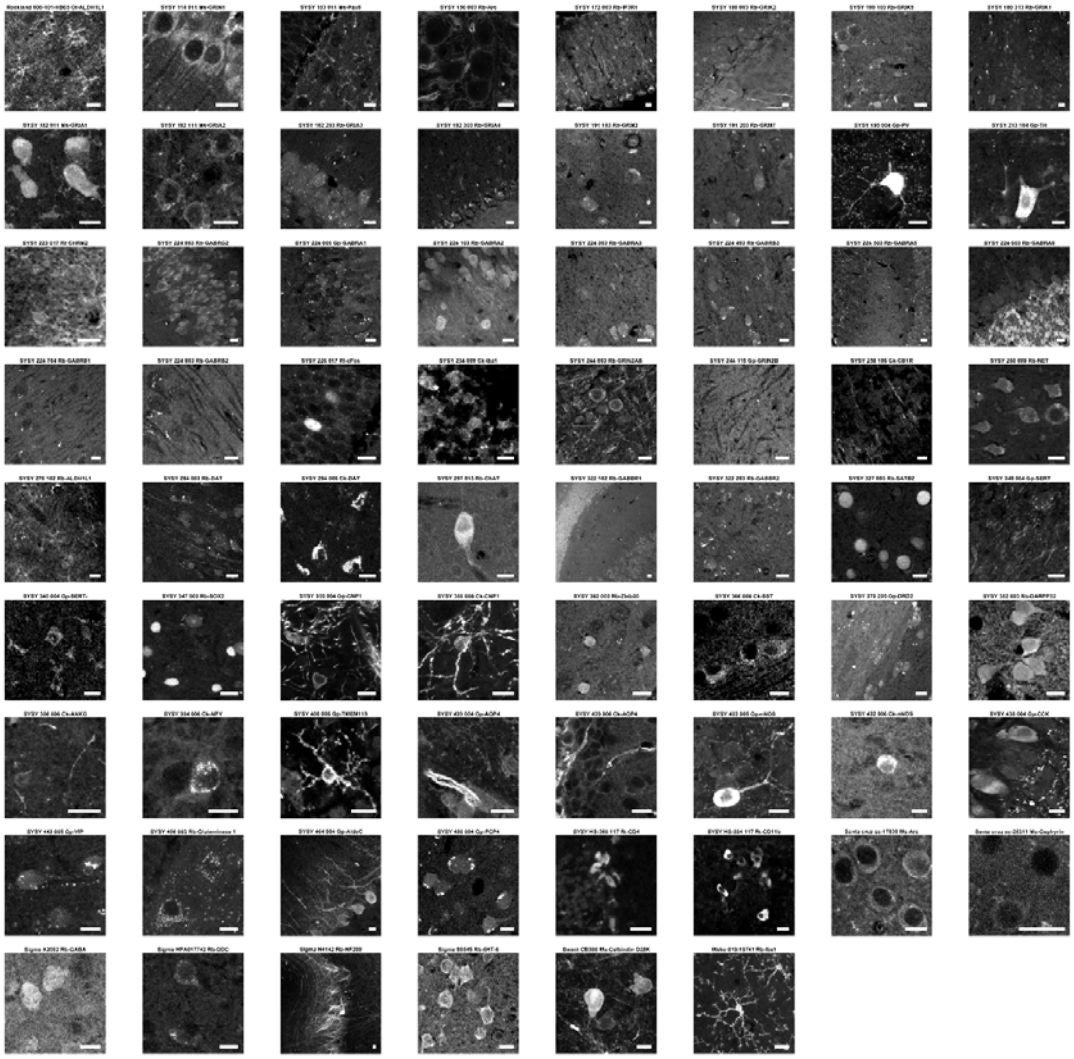

Figure S7. Representative images from INSIHGT-compatible antibodies, Part 3. Scale bars are set to 10 µm.

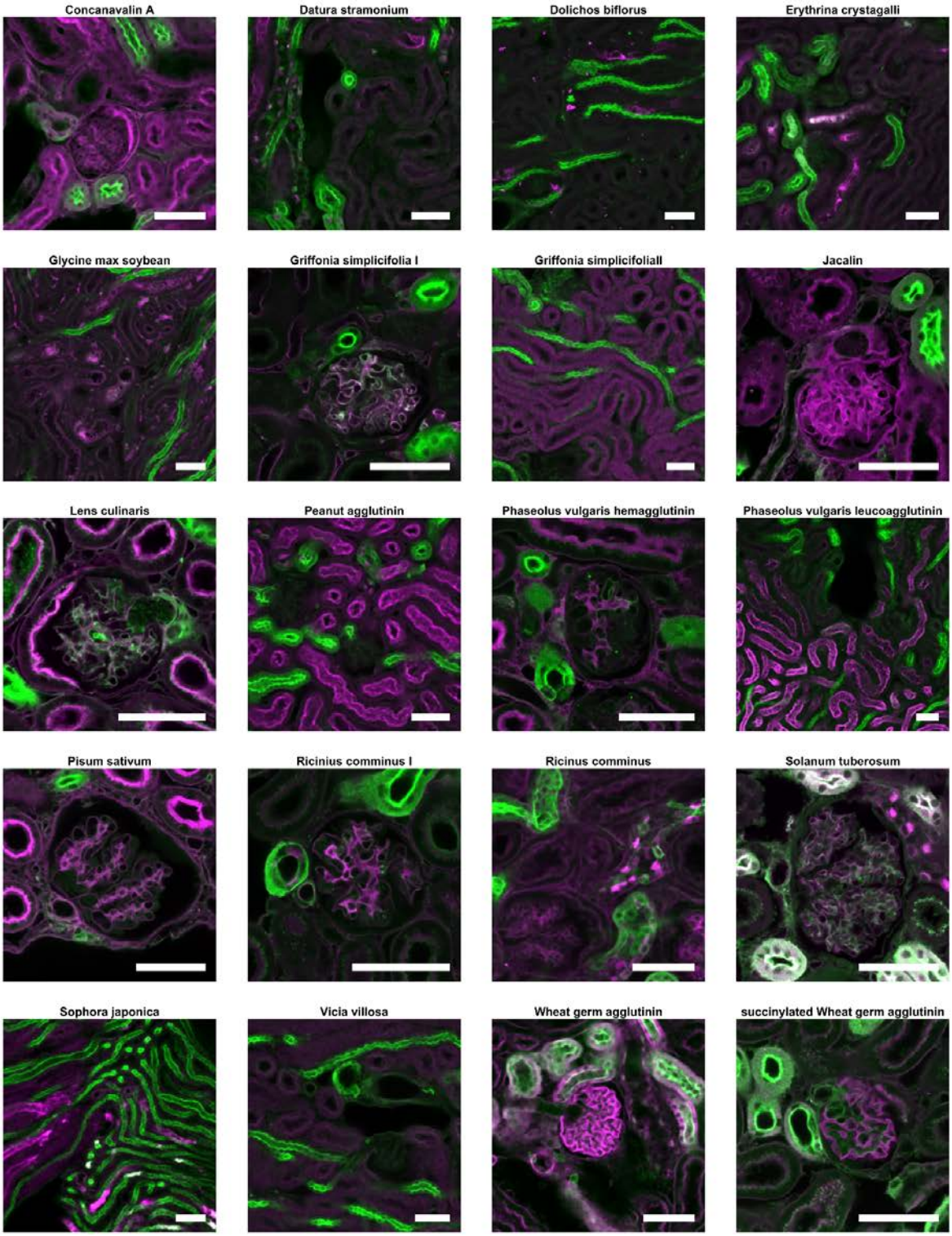

Figure S8. Representative images of lectins histochemistry compatible with INSIHGT performed on mouse kidney tissue. Shown in magenta are the titled lectin's signals. The signals from *Lycopersicon esculentum* lectin are shown in green for orientation. Scale bars are set to 50 µm.

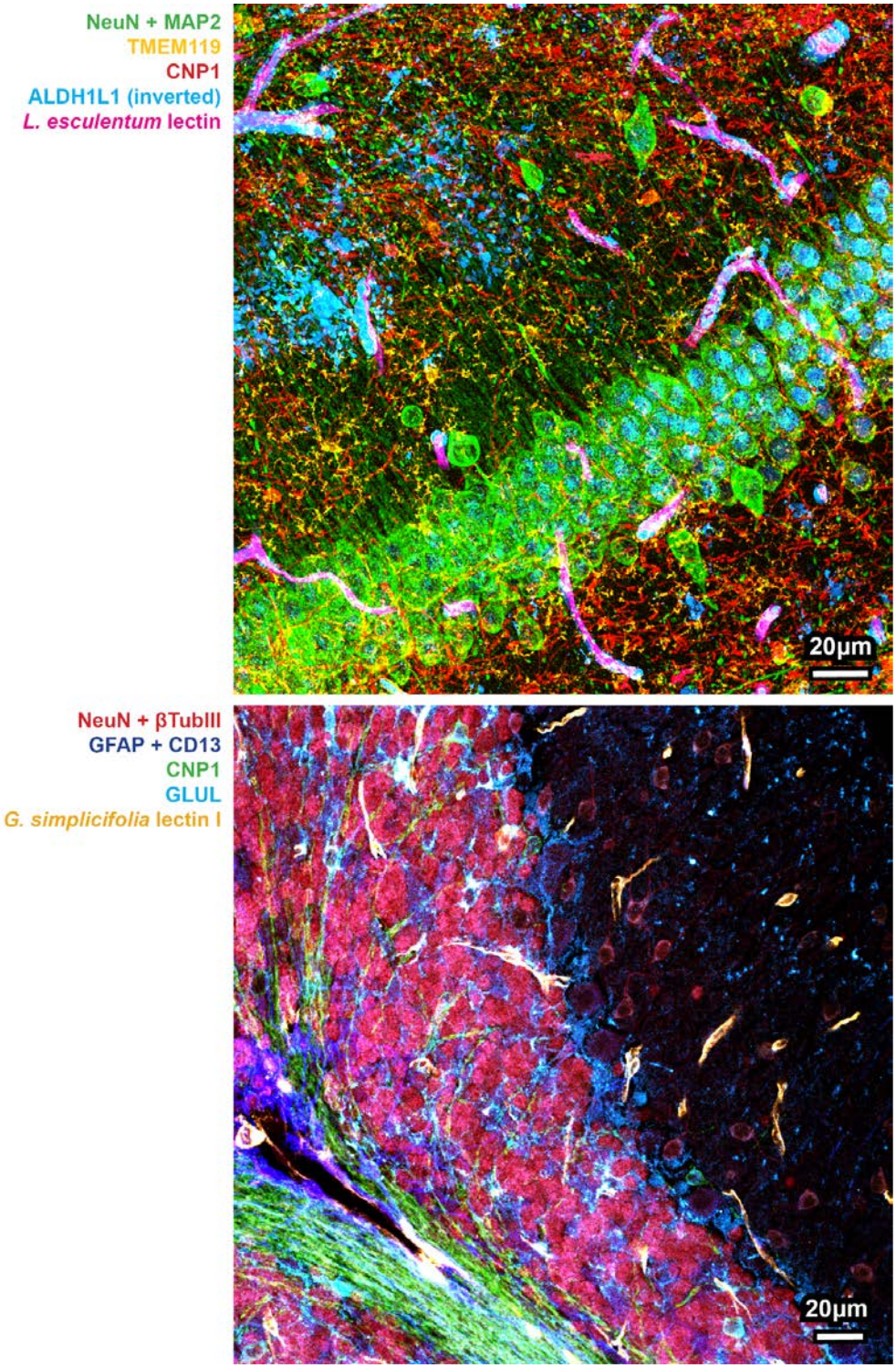

Figure S9. Multiplexing with INSIHGT with high concentrations of antibodies. Upper image: mouse hippocampus stained with 6 protein probes, lower image: mouse cerebellum stained with 7 protein probes. The signal of ALDH1L1 was inverted due to the ubiquitous homogeneous staining of the original signal.

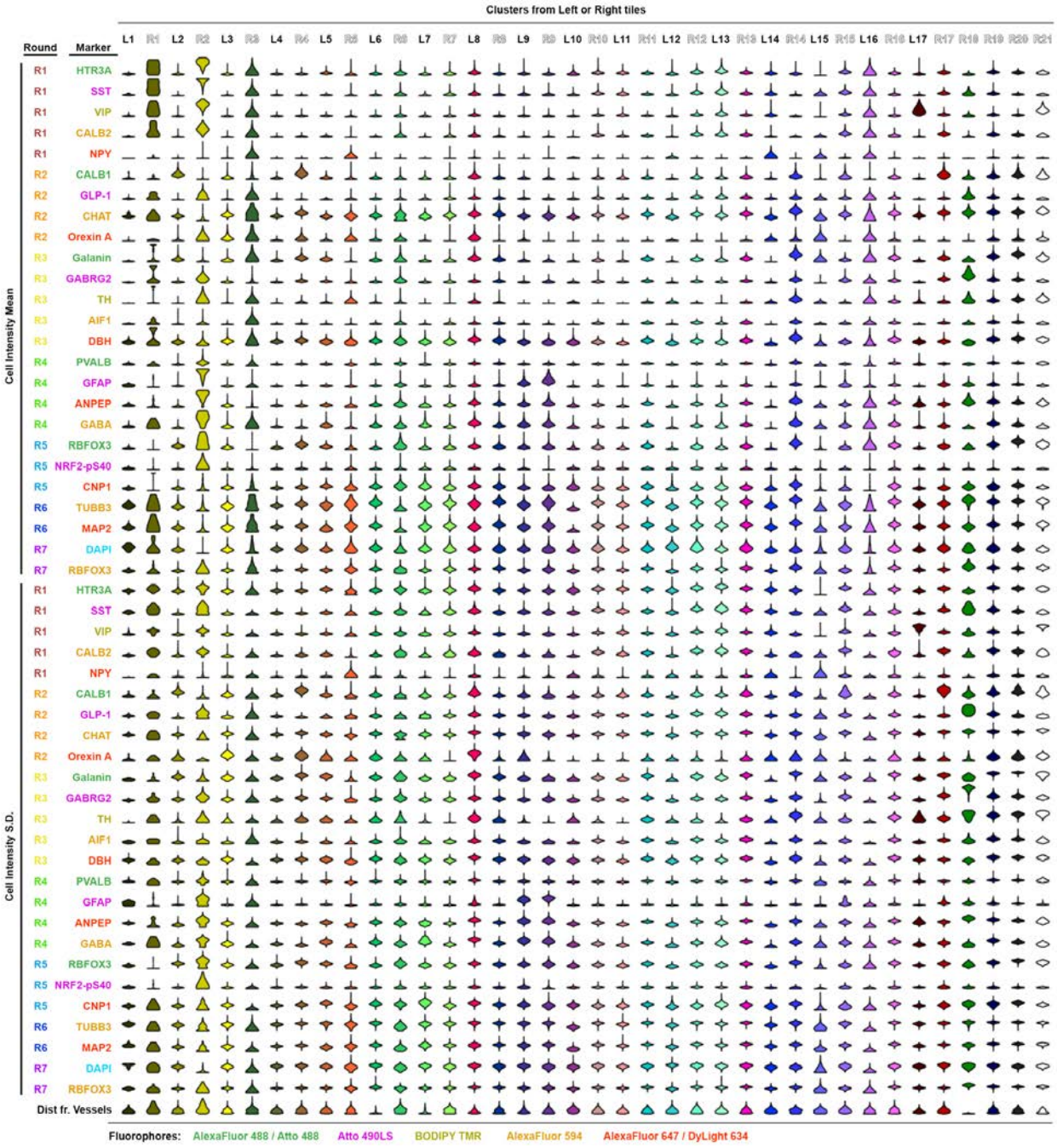

Figure S10. Violin Plots of Each Marker. These plots represent immunostaining mean intensities and their standard deviations (SDs), separately, and the distance from vessels for each cluster obtained by nested UMAP analysis in **Figure 4**. The text is color-coded based on the fluorophore used in the imaging experiment.

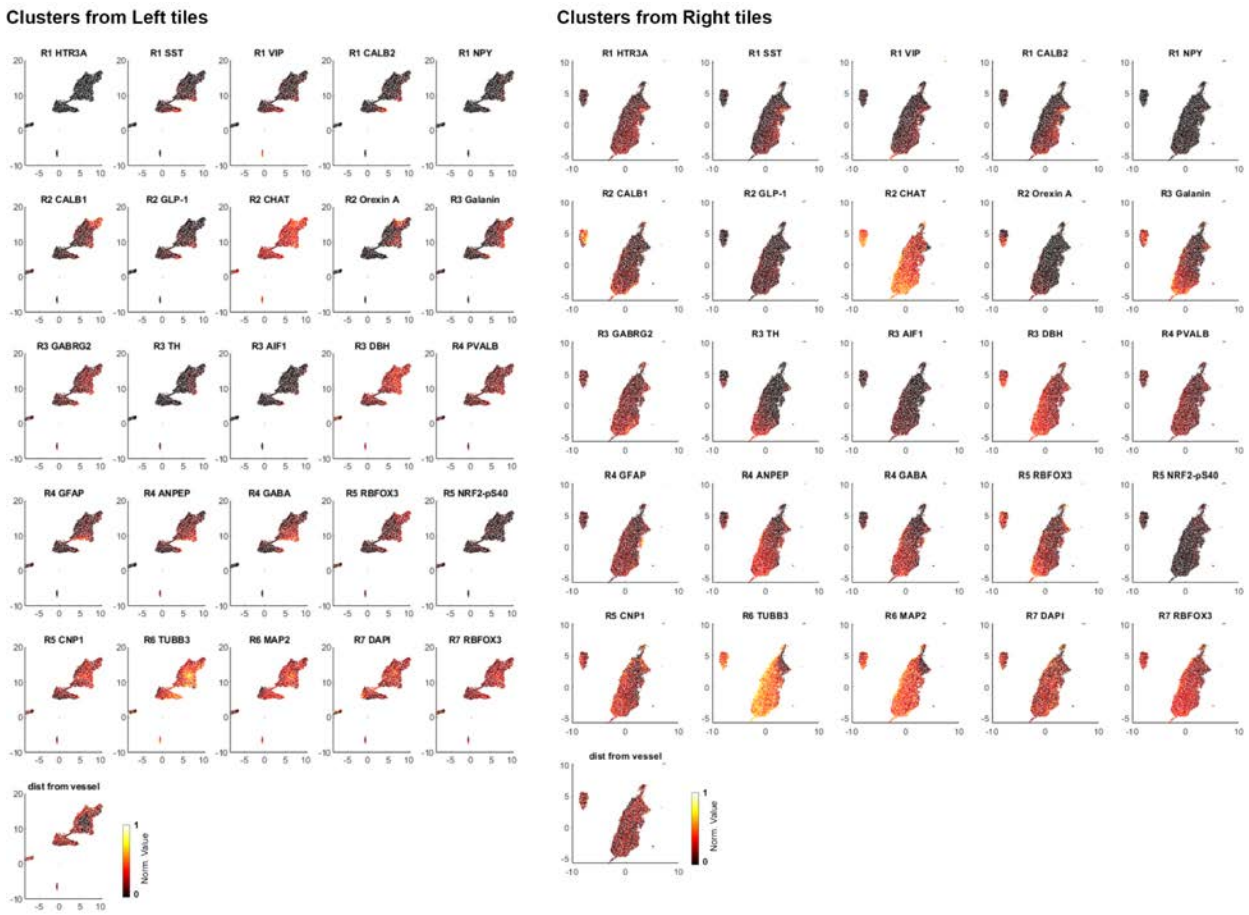

Fig. S11. The mean immunostaining intensities of each marker in a 2D-embedded UMAP space.

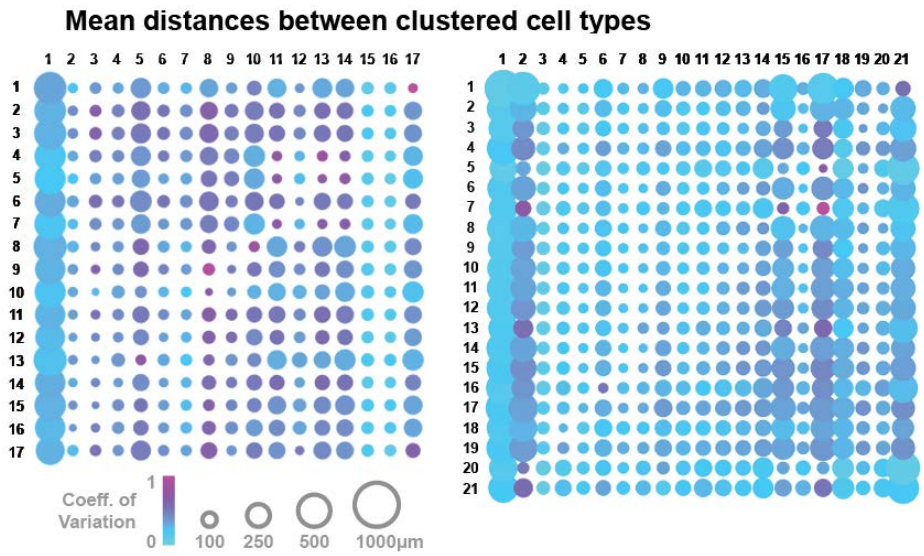

Figure S12. Mean nearest distance matrix between each cell type from each cluster. The size of the dot plot represents the coefficient of variation.

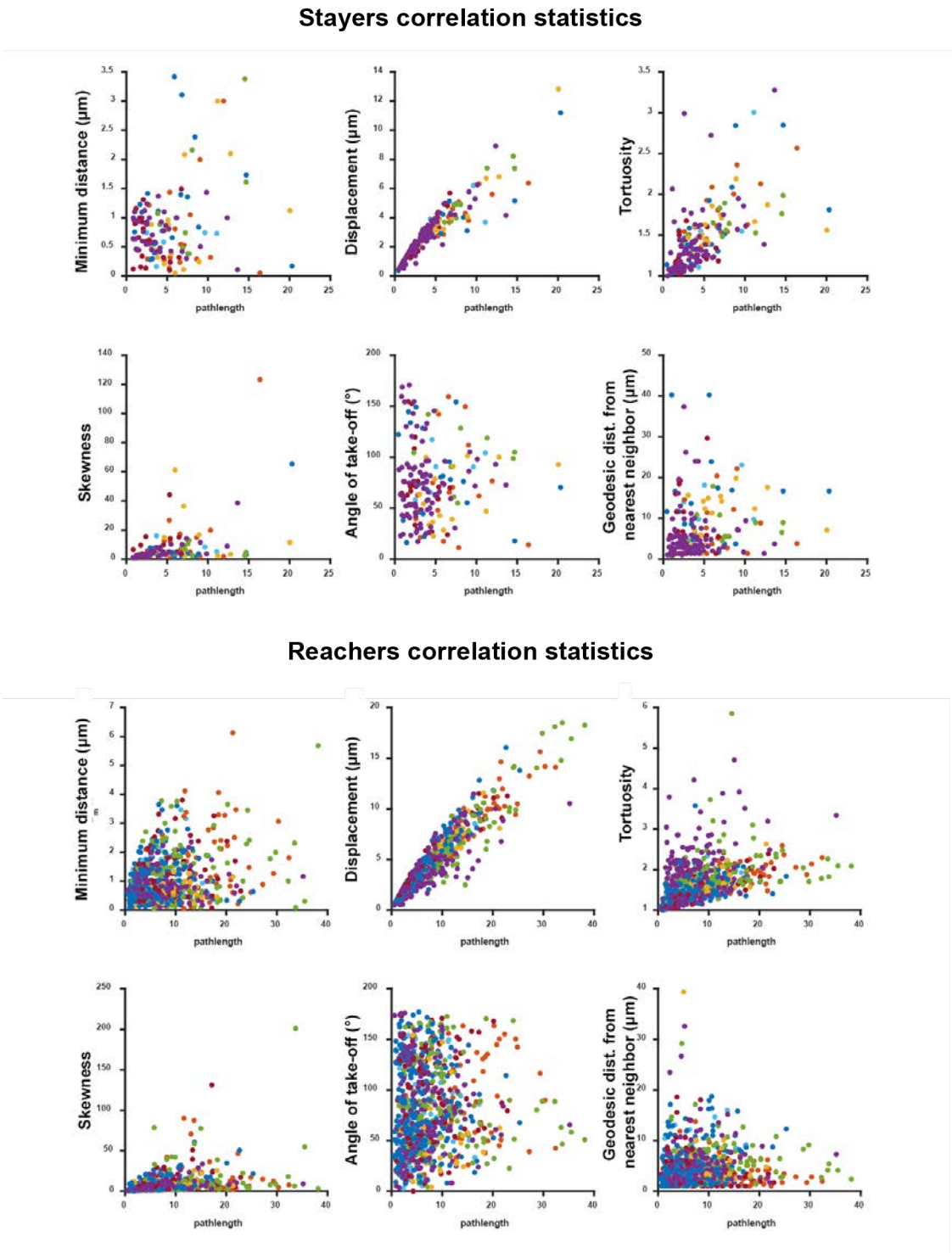

Figure S13. Correlation statistics of physical parameters obtained from 3D images of mouse kidneys, for reacher and stayer clusters respectively (see also **Figure** 7).

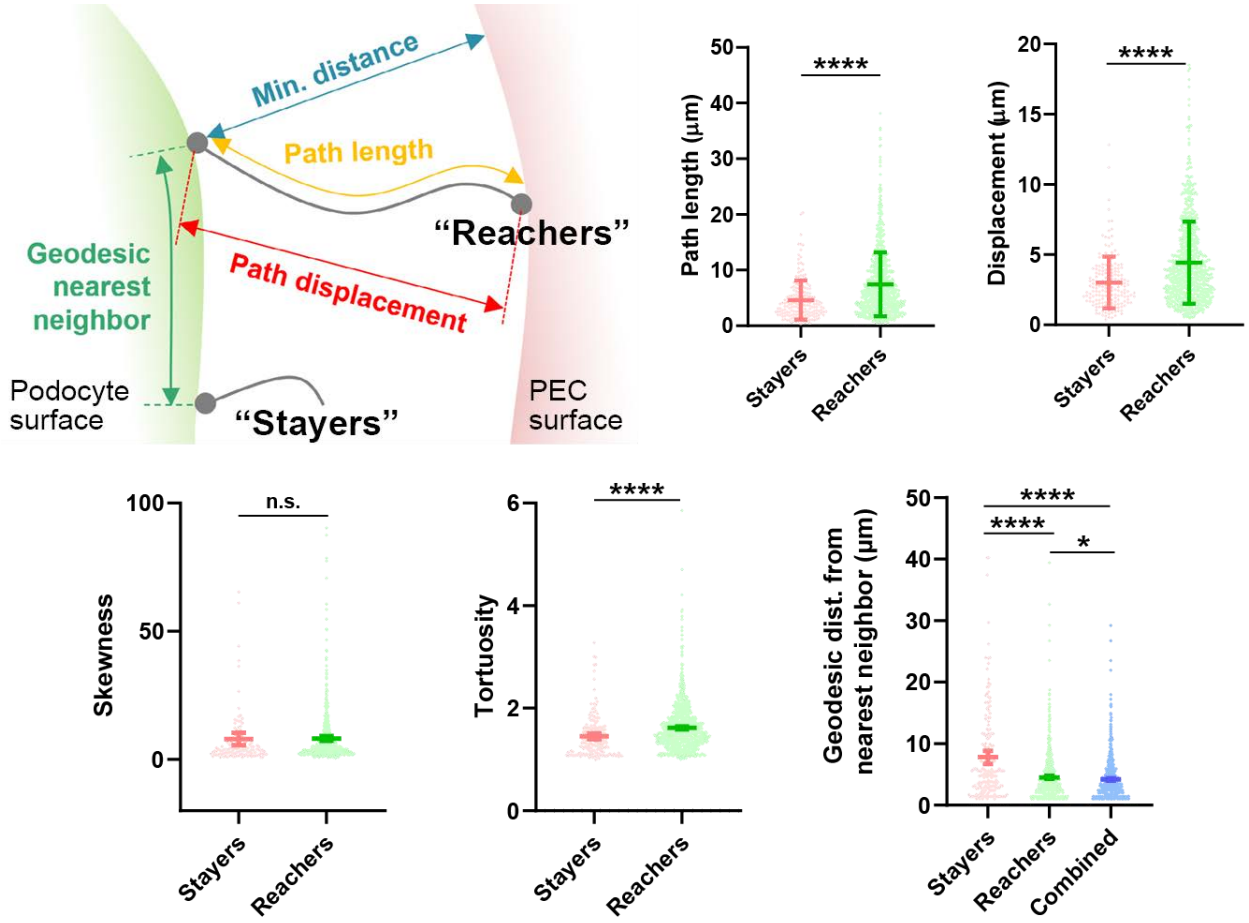

Figure S14. Comparison of morphological and spatial parameters between stayers and reachers clusters obtained from 3D images of mouse kidneys (****: $p < 0.0001$).

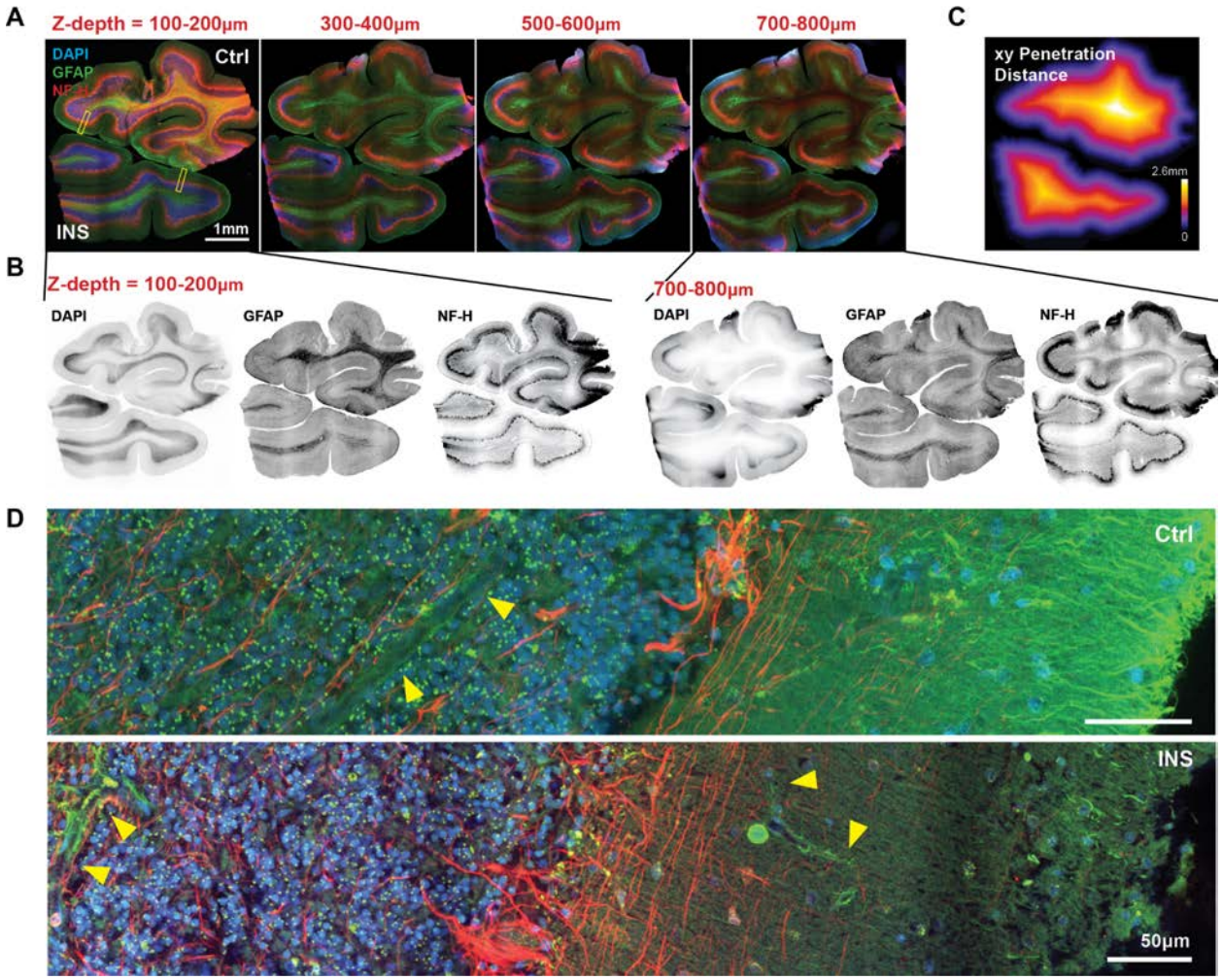

Figure S15. (**A**) Direct comparison of INSIHGT with iDISCO (Ctrl) in human cerebellum tissues of size 3 mm × 4 mm × 2 mm across various Z-depths. (**B**) Individual view of each channel in (**A**) at the indicated Z-depths. (**C**) Distance-transformed penetration distance at the highest Z-depth. (**D**) Enlarged views from (**A**) show superior staining quality that more accurately reflects antigen distribution. This includes a high intensity of GFAP (in green) signal in the granular layer rather than the molecular layer and their presence around vessels (yellow arrowheads), deeper penetration and clearer signal for nuclei (in blue) for [DAPI⊂SBEβCD] compared with DAPI only (in Ctrl), and crisper neurofilament staining (in red) in INSIHGT, particularly in the deeper layers.

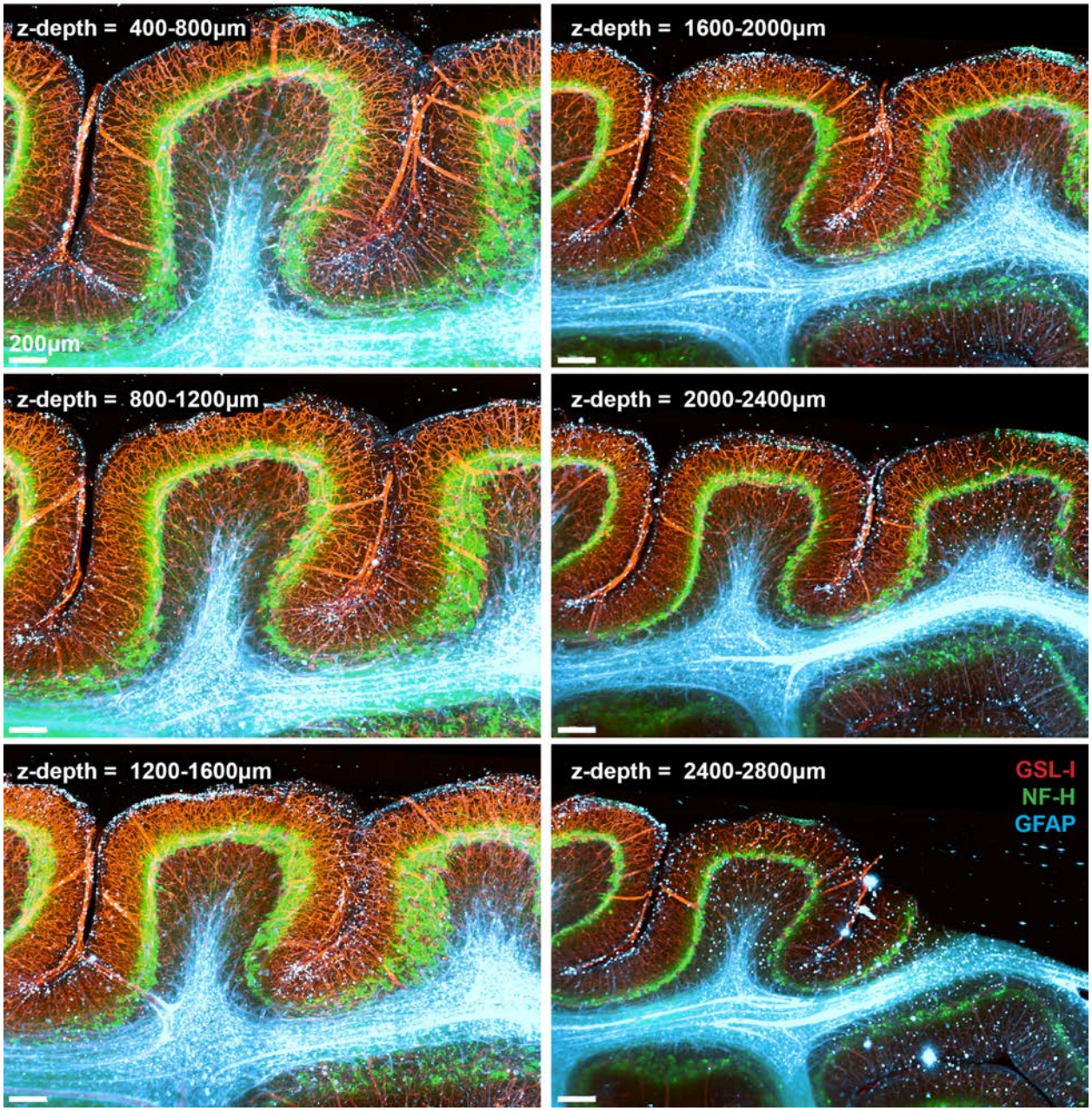

Figure S16. Series of Z-projections of the 4mm × 8mm × 3mm human cerebellum triplex stained for vessels (with *Griffonia simplicifolia* lectin I, GSL-I, in red), neurofilaments (NF-H, in green), and astrocytes (GFAP, in blue).

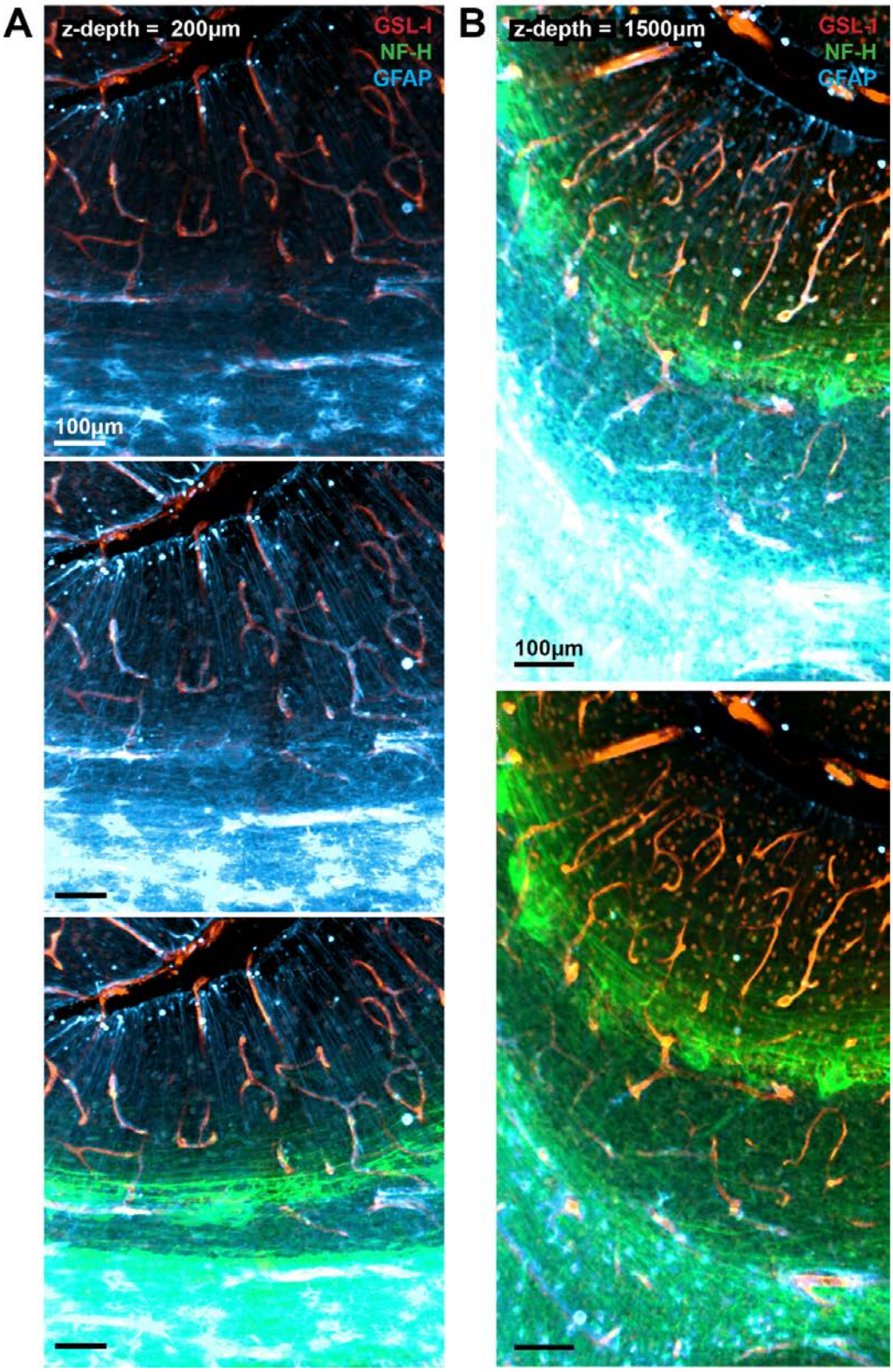

Figure S17. Zoomed-in view of the light-sheet microscopy image in **Figure S13**. Showing details such as astrocytic endfeets around blood vessels, Bergmann glia processes, and neurofilament fibres in all 3 layers at different *z*-depths. The images were rendered in different dynamic ranges to facilitate visualization of one layer over the other.

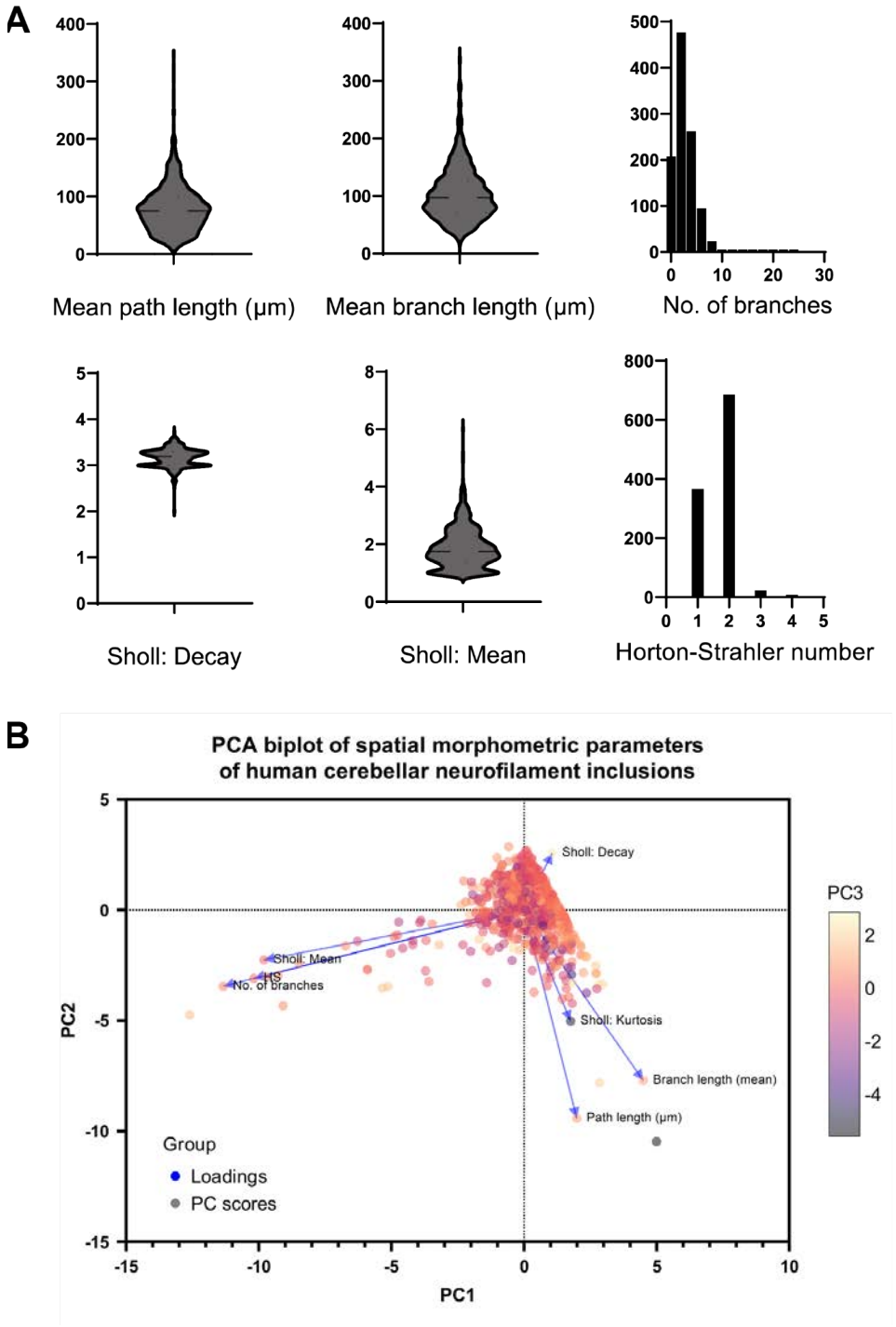

Figure S18. Descriptive statistics of physical parameters obtained from 3D images of human cerebellar neurofilament inclusions, with subsequent principle component analysis with selected parameters (see also **Figure 8**).

Supplementary Movies

Movie S1. 3D visualization of the 3 mm-thick, 3-plex immunostained human cerebellum in **Fig. 8** and **Fig. S16-17.**

Table S1. Antibody penetration exponential decay constant of benchmarking experiment using mouse hemi-brains as an estimate of signal inhomogeneity.

	Inhomogeneity, $\tau \times 10^3$ (confidence interval)
INSIHGT	2.7 (1.7, 3.7)
CUBIC-HV	24.7 (23.3, 26.1)
eFLASH	227.8 (210.7, 244.9)
iDISCO	48.6 (44.8, 52.4)
SHANEL	5.5 (5.2, 5.7)
SWITCH-ELAST	136.6 (122.8, 150.4)

Table S2. List of antibodies tested with INSIHGT.

Supplier	Cat. no.	Antigen	Host	Compatible
Santa cruz	sc-365529	11bHSD2	Ms	No
Abclonal	A12391	AIF1/IBA1	Rb	No
DSHB	N106/65	ANKG	Ms	No
Abclonal	A2887	AQP4	Rb	No
Abclonal	A12289	beta-tubulin	Rb	No
Abclonal	A18275	CARTPT	Rb	No
SantaCruz	sc-166940	c-Fos	Ms	No
DSHB	K55/7	ChIP1	Ms	No
Aves	CNP	CNP1	Ck	No
Abclonal	A18028	Cry1	Rb	No
Abclonal	A3019	CSF1R	Rb	No
Abcam	ab216588	Cux2	Rb	No
Sigma	HPA002130	DBH	Rb	No
Sigma	HPA001733	DLG3	Rb	No
Abclonal	A12930	DRD2	Rb	No
Abclonal	A1556	DRD3	Rb	No
DSHB	Mab3F52	GLP1R	Ms	No
DSHB	L21/32	GRIA2	Ms	No
Abclonal	A5465	HDC	Rb	No
Abcam	ab5076	Iba1	Gt	No
Abclonal	A0303	IGF1	Rb	No
Abcam	ab133474	LRRK2	Rb	No
Abclonal	A1664	MBP	Rb	No
SYSY	260 308	NET/SLC6A2	Gp	No

AbClonal	A3048	NPHS1	Rb	No
Abcam	ab50339	NPHS2	Rb	No
Abclonal	A12814	Olig2	Rb	No
Abclonal	A20009	PLP1	Rb	No
Sigma	P0372	Podocin	Rb	No
Abclonal	A14171	SERT/SLC6A4	Rb	No
Abclonal	A2799	SLC18A2/VMAT2	Rb	No
DSHB	PCRP-SOX2-1B3	SOX2	Ms	No
Sigma	AMab91108	TPH2	Ms	No
Abclonal	A14472	TRH	Rb	No
Sigma	AMAB91081	VGLUT2	Ms	No
Sigma	S5545	5-HT	Rb	Yes
Immusmol	IS040	5-HT	Ms	Yes
Abclonal	A7255	Acetyl-Histone-H3-K9	Rb	Yes
Abclonal	A2525	ADAMTS4	Rb	Yes
Abclonal	A1471	ADRA1A	Rb	Yes
Abclonal	A2809	ADRA2A	Rb	Yes
Abclonal	A16334	ADRB1	Rb	Yes
Abclonal	A2048	ADRB2	Rb	Yes
Abclonal	A12192	AGMAT	Rb	Yes
Abclonal	A8044	AGRP	Rb	Yes
Abclonal	A15637	Agt	Rb	Yes
Abclonal	A12326	Agt	Rb	Yes
Rockland	600-101-HB65	ALDH1L1	Gt	Yes
Abcam	ab56777	ALDH1L1	Ms	Yes
Proteintech	17390-1-AP	ALDH1L1	Rb	Yes
SYSY	278 102	ALDH1L1	Rb	Yes
Abclonal	A11618	ALDOC	Rb	Yes
SYSY	464 004	Aldolase C	Gp	Yes
Abclonal	A13354	Alpha synuclein	Rb	Yes
Abclonal	A20407	Alpha synuclein	Rb	Yes
BD	610787	Alpha synuclein	Ms	Yes
Abcam	ab184674	Alpha synuclein pS129	Ms	Yes
SYSY	386 006	Ankyrin G	Ck	Yes
Abclonal	A4195	AQP1	Rb	Yes
Abclonal	A16209	AQP2	Rb	Yes
SYSY	429 006	AQP4	Ck	Yes
SYSY	429 004	AQP4	Gp	Yes
Alomone Labs	AQP-005	AQP5	Rb	Yes
Santa cruz	sc-17839	Arc	Ms	Yes
Synaptic systems	156 003	Arc	Rb	Yes
Abclonal	A1223	ARHGAP25	Rb	Yes

Invitrogen	MA1-06110	aSMA	Ms	Yes
Abclonal	A17910	aSMA	Rb	Yes
Progen	690001	aSMA	Rb	Yes
Abclonal	A11217	ATP5A1	Rb	Yes
Abclonal	A4873	BDNF	Rb	Yes
Abcam	ab78078	bIIITub	Ms	Yes
Abcam	ab11862	C3	Rt	Yes
Abclonal	A1212	CA3	Rb	Yes
SYSY	214 011	Calbindin	Ms	Yes
AbClonal	A4284	Calbindin	Rb	Yes
CST	13176S	Calbindin	Rb	Yes
Swant	CB300	Calbindin D28K	Ms	Yes
Abclonal	A11979	CALCRL	Rb	Yes
R&D	AF5065	Calretinin	Gt	Yes
Abclonal	A0198	CaMKII	Rb	Yes
Origene	TA808345	CaMKIIb	Ms	Yes
DSHB	PCRP-CAMKK2-1H7	CAMKK2b	Ms	Yes
DSHB	K65/35-s	CASPR/Neurexin IV	Ms	Yes
SYSY	258 106	CB1R	Ck	Yes
SYSY	438 004	CCK	Gp	Yes
Abclonal	A1759	CCK	Rb	Yes
SYSY	HS-360 117	CD4	Rt	Yes
SYSY	HS-384 117	CD11b/ITGAM	Rt	Yes
Abclonal	A1508	CD11c/ITGAX	Rb	Yes
Abclonal	A5662	CD13	Rb	Yes
Abclonal	A11669	CD13	Rb	Yes
Jotbody	AP01388a	CD19	Rb	Yes
Abclonal	A12711	CD133	Rb	Yes
Abclonal	A4900	CD31-PECAM1	Rb	Yes
Abclonal	A0761	CD34	Rb	Yes
LSBio	LS-C359273	CD44	Ms	Yes
Abclonal	A15995	CENP-A	Rb	Yes
Abclonal	A16641	c-Fos	Rb	Yes
Abclonal	A0236	c-Fos	Rb	Yes
CST	2250S	c-Fos	Rb	Yes
SYSY	226 017	c-Fos	Rt	Yes
Abclonal	A5542	CGRP	Rb	Yes
Millipore	AB144	ChAT	Gt	Yes
Invitrogen	MA3-31382	ChAT	Ms	Yes
Abclonal	A13244	ChAT	Rb	Yes
SYSY	297 013	ChAT	Rb	Yes
DSHB	K60/73	ChIP2	Ms	Yes

DSHB	K66/38	ChIP3	Ms	Yes
SYSY	223 017	CHRM2	Rt	Yes
Abclonal	A1602	CHRM3	Rb	Yes
Abclonal	A3792	CLCNKA	Rb	Yes
SYSY	355 006	CNP1	Ck	Yes
SYSY	355 004	CNP1	Gp	Yes
Abclonal	A20483	CTIP/BCL11B	Rb	Yes
Abclonal	A2160	CYP2E1	Rb	Yes
Abclonal	A2544	CYP3A4	Rb	Yes
SYSY	382 003	DARPP32	Rb	Yes
Millipore	MAB369	DAT	Rb	Yes
SYSY	284 006	DAT	Ck	Yes
SYSY	284 003	DAT/SLC6A3	Rb	Yes
Abcam	ab189991	DBH	Gt	Yes
Abclonal	A13971	DBH	Rb	Yes
Invitrogen	PA3-925	DBH	Sh	Yes
Abclonal	A3828	DDC	Rb	Yes
Sigma	HPA017742	DDC	Rb	Yes
Abcam	ab167612	DeltaNp63	Ms	Yes
Immusmol	IS1005	Dopamine	Rb	Yes
Abclonal	A2893	DRD1	Rb	Yes
SYSY	376 205	DRD2	Gp	Yes
Millipore	205604	E-Cadherin	Rt	Yes
Abcam	ab41621	EAAT2	Rb	Yes
Abclonal	A2722	EGR1	Rb	Yes
Abcam	ab204991	ELAVL2	Rb	Yes
Invitrogen	MA5-26826	FEZF2	Ms	Yes
Abcam	ab205606	Flag	Rb	Yes
DSHB	PCRP-FOXA2-3A2	FOXA2	Ms	Yes
DSHB	PCRP-FOXP4-1G7	FOXP4	Ms	Yes
Immusmol	IS1036	GABA	Ck	Yes
Sigma	A2052	GABA	Rb	Yes
Sigma	HPA055746	GABARA1	Rb	Yes
SYSY	322 102	GABBR1	Rb	Yes
SYSY	322 203	GABBR2	Rb	Yes
SYSY	224 205	GABRA1	Gp	Yes
SYSY	224 103	GABRA2	Rb	Yes
SYSY	224 303	GABRA3	Rb	Yes
DSHB	GABRA4-R24	GABRA4	Rb	Yes
SYSY	224 503	GABRA5	Rb	Yes
SYSY	224 603	GABRA6	Rb	Yes
SYSY	224 703	GABRB1	Rb	Yes

SYSY	224 803	GABRB2	Rb	Yes
SYSY	224 403	GABRB3	Rb	Yes
SYSY	224 003	GABRG2	Rb	Yes
DSHB	GABRG3-R21	GABRG3	Rb	Yes
Abcam	ab111070	GAD1/2	Rb	Yes
Abclonal	A0971	GAD2	Rb	Yes
Abclonal	A14609	GCG	Rb	Yes
SantaCruz	sc-25311	Gephyrin	Ms	Yes
Aves	GFAP	GFAP	Ck	Yes
Dako	M0761	GFAP	Ms	Yes
Invitrogen	13-0300	GFAP	Rt	Yes
Abcam	ab252881	GFP	Gt	Yes
Abcam	ab6673	GFP	Rt	Yes
Invitrogen	PA5-47769	GFRAL	Sh	Yes
Abclonal	A4981	GLP1	Rb	Yes
Abclonal	A4981	GLP1	Rb	Yes
DSHB	Mab7F38	GLP1R	Ms	Yes
Abclonal	A8547	GLP1R	Rb	Yes
SYSY	367 005	GLUL	Gp	Yes
Immusmol	IS1002	D-Glutamate	Rb	Yes
Immusmol	IS1001	L-Glutamate	Rb	Yes
SYSY	456 003	Glutaminase 1	Rb	Yes
Immusmol	IS1034	Glycine	Rb	Yes
Abclonal	A11408	GM130	Rb	Yes
Abclonal	A5625	GNRH1	Rb	Yes
SYSY	182 011	GRIA1	Ms	Yes
AbClonal	A1826	GRIA1	Rb	Yes
SYSY	182 111	GRIA2	Ms	Yes
SYSY	182 203	GRIA3	Rb	Yes
SYSY	182 303	GRIA4	Rb	Yes
SYSY	180 313	GRIK1	Rb	Yes
AbClonal	A9722	GRIK2	Rb	Yes
SYSY	180 003	GRIK2	Rb	Yes
SYSY	180 203	GRIK3	Rb	Yes
SYSY	180 103	GRIK5	Rb	Yes
SYSY	114 011	GRIN1	Ms	Yes
DSHB	327/95	GRIN2A	Ms	Yes
SYSY	244 003	GRIN2A/B	Rb	Yes
SYSY	244 115	GRIN2B	Gp	Yes
DSHB	N59/36	GRIN2B	Ms	Yes
AbClonal	A3056	GRIN2B	Rb	Yes
SYSY	191 103	GRM2	Rb	Yes

SYSY	191 203	GRM7	Rb	Yes
AbClonal	A2964	GRM8	Rb	Yes
Abclonal	A7253	H3K27ac	Rb	Yes
Abclonal	A2361	H3K27me	Rb	Yes
Abclonal	A2362	H3K27me2	Rb	Yes
Abclonal	A2363	H3K27me3	Rb	Yes
Abclonal	A7255	H3K9Ac	Rb	Yes
Abclonal	A3156	H3R8me	Rb	Yes
Abclonal	A3157	H3R8me2-asymmetric	Rb	Yes
Abclonal	A21207	H3R8me2-symmetric	Rb	Yes
DSHB	N70/28	HCN1	Ms	Yes
DSHB	N114/10	HCN4	Ms	Yes
Immunsmol	IS1039	Histamine	Rb	Yes
Abclonal	A3692	Histone H2A	Rb	Yes
Abclonal	A17813	Histone H2A.V	Rb	Yes
Abclonal	A12442	Histone H2A.Z	Rb	Yes
Abclonal	A11540	Histone H2AX	Rb	Yes
Abclonal	A4835	Histone H3.3	Rb	Yes
Abclonal	A11252	HLA-DQA1	Rb	Yes
Abclonal	A8077	HSD11B2	Rb	Yes
Abclonal	A2801	HTR1A	Rb	Yes
Abclonal	A18285	HTR1B	Rb	Yes
Abclonal	A14743	HTR1F	Rb	Yes
Abclonal	A20538	HTR2A	Rb	Yes
Immunostar	24288	HTR2A	Rb	Yes
AbClonal	A5647	HTR3A	Rb	Yes
Abclonal	A2802	HTR4	Rb	Yes
Abclonal	A19706	HTR7	Rb	Yes
SYSY	234 009	Iba1	Ck	Yes
Wako	019-19741	Iba1	Rb	Yes
SYSY	117 002	IP3R type 1	Rb	Yes
R&D	AF599	Jagged1	Gt	Yes
DSHB	L18A/3	KCNMB4	Ms	Yes
Abclonal	A17061	KEAP1	Rb	Yes
DSHB	N112B/14	Kir2.1	Ms	Yes
Abclonal	A1024	KRT8/TROMA-1	Rb	Yes
DSHB	SP2/0	KRT8/TROMA-1	Rt	Yes
Abclonal	A0247	KRT19	Rb	Yes
DSHB	K36/15	Kv1.1	Ms	Yes
DSHB	K14/16	Kv1.2	Ms	Yes
DSHB	K89/34	Kv2.1	Ms	Yes
DSHB	K37/89	Kv2.2	Ms	Yes

DSHB	K57/1	Kv4.2	Ms	Yes
DSHB	K9/40	Kvb1.1	Ms	Yes
DSHB	K17/70	Kvb2	Ms	Yes
AbClonal	A19970	Laminin b1	Rb	Yes
Abclonal	A2999	LEPR	Rb	Yes
Abclonal	A7045	macroH2A.1	Rb	Yes
Abclonal	A2572	MAP2	Rb	Yes
SYSY	188 011BT	MAP2	Ms	Yes
Abcam	ab24233	MC4R	Rb	Yes
Abclonal	A10228	MC4R	Rb	Yes
Abclonal	A3013	MCT1/SLC16A1	Rb	Yes
AbClonal	A3673	mGluR2	Rb	Yes
Abcam	ab206486	Myc	Rt	Yes
DSHB	PCRP-MYCN-1A9	MYCN	Ms	Yes
AbClonal	A11683	NaK-ATPase	Rb	Yes
DSHB	K69/3	Nav1.2	Ms	Yes
DSHB	K87A/10	Nav1.6	Ms	Yes
Abclonal	A1421	NET/SLC6A2	Rb	Yes
SYSY	260 008	NET/SLC6A2	Rb	Yes
Abcam	ab104224	NeuN	Ms	Yes
Abclonal	A19086	NeuN	Rb	Yes
AbClonal	A19084	Neurofilament-H	Rb	Yes
Sigma	N4142	Neurofilament-H	Rb	Yes
AbClonal	A0257	Neurofilament-L	Rb	Yes
AbClonal	A19085	Neurofilament-M	Rb	Yes
Abclonal	A12326	Neurotensin	Rb	Yes
AbClonal	A11699	NMDAR1	Rb	Yes
AbClonal	A0924	NMDAR2A	Rb	Yes
SYSY	432 006	nNOS	Ck	Yes
SYSY	432 005	nNOS	Gp	Yes
Abclonal	A8319	NOL3/Arc	Rb	Yes
Immusmol	IS1042	L-Noradrenaline	Rb	Yes
Invitrogen	PA5-39300	NPAS4	Rb	Yes
SYSY	394 006	NPY	Ck	Yes
Abclonal	A3178	NPY	Rb	Yes
DSHB	PCRP-NRF1-3D4	NRF1	Ms	Yes
Abclonal	AP1133	NRF2-pS40	Rb	Yes
AbClonal	A2029	NT5E	Rb	Yes
Abclonal	A12326	NTS	Rb	Yes
Millipore	AB3704	Orexin A	Rb	Yes
Jotbody	0112	p53	Ap	Yes
DSHB	N419/40	Pan-Na.v1	Ms	Yes

Abcam	ab18257	PARK7	Rb	Yes
Abcam	ab179812	Parkin	Rb	Yes
DSHB	PCRP-PAX2-1A7	Pax2	Ms	Yes
SYSY	153 011	Pax6	Ms	Yes
SYSY	480 004	PCP4	Gp	Yes
AbClonal	A2103	PDGFRA	Rb	Yes
AbClonal	A19531	PDGFRB	Rb	Yes
Abclonal	AP1022	PDH-pS293	Rb	Yes
CST	37115	PDH-pS293	Rb	Yes
Jotbody	0002	PD-L1	Ap	Yes
Abclonal	A5830	PDYN	Rb	Yes
Abclonal	AP0687	Phospho-Histone-H2AX-S139	Rb	Yes
Abclonal	AP0093	Phospho-Histone-H3-T11	Rb	Yes
CST	4370S	Phospho-p44/42 MAPK	Rb	Yes
Invitrogen	44-923G	Phospho-S6(S244,S247)	Rb	Yes
Abclonal	A9655	Phox2b	Rb	Yes
Abcam	ab186303	PINK1	Ms	Yes
Abclonal	A10200	PODXL	Rb	Yes
NeuroMab	75-028	PSD95	Ms	Yes
SYSY	195 004	PVALB	Gp	Yes
Abcam	ab32895	PVALB	Gt	Yes
Abclonal	A19098	PVALB	Rb	Yes
Invitrogen	PA1-933	PVALB	Rb	Yes
Abclonal	A19710	SOX9	Rb	Yes
Abclonal	A10029	RBP1	Rb	Yes
Abclonal	A17936	RELN	Rb	Yes
Abclonal	A1585	Renin	Rb	Yes
Abcam	ab125244	RFP	Ms	Yes
Abclonal	A19753	RORbeta	Rb	Yes
Enzo	ENZ-ABS307-0100	S100b	Rb	Yes
DSHB	N19/2	SAP102	Ms	Yes
SYSY	327 003	SATB2	Rb	Yes
Abclonal	A15097	scnn1g	Rb	Yes
SYSY	340 004	SERT	Gp	Yes
SYSY	340 004	SERT/SLC6A4	Gp	Yes
Abclonal	A12999	slc12a1	Rb	Yes
Abclonal	A18382	slc12a3	Rb	Yes
Abclonal	A15991	slc14a1	Rb	Yes
Abclonal	A13208	slc14a2	Rb	Yes
Abclonal	A15177	SLC17A6 (VGLUT2)	Rb	Yes
Abclonal	A12879	SLC17A7	Rb	Yes
Abclonal	A2799	SLC18A2	Rb	Yes

LSBio	LS-B6724	SLC1A2	Ms	Yes
Abclonal	A1814	SLC22A6	Rb	Yes
Abclonal	A20271	SLC5A2	Rb	Yes
Invitrogen	PA5-101896	SLC5A3	Rb	Yes
Abclonal	A17532	Slc9a3	Rb	Yes
AbClonal	A19576	SOD2	Rb	Yes
Abcam	ab97959	SOX2	Rb	Yes
SYSY	347 003	SOX2	Rb	Yes
SYSY	366 006	SST	Ck	Yes
AbClonal	A9274	SST	Rb	Yes
Millipore	MAB354	SST	Rt	Yes
R&D	MAB2358	SST	Gt	Yes
Novus	NB300-104	Synapsin I	Rb	Yes
Abclonal	A13550	Tac1	Rb	Yes
Abclonal	A6312	TAC3	Rb	Yes
Abcam	A121690	tdTomato	Gt	Yes
Abclonal	A5865	TFRC	Rb	Yes
SYSY	213 104	TH	Gp	Yes
Abclonal	A0028	TH	Rb	Yes
Millipore	AB152	TH	Rb	Yes
SYSY	400 006	TMEM119	Gp	Yes
Abcam	ab209064	TMEM119	Rb	Yes
Abclonal	A7147	TPH2	Rb	Yes
Abclonal	A10482	TREM2	Rb	Yes
DSHB	N67/15	TRPC5	Ms	Yes
Novus Biologicals	NBP1-80651	UBAP1	Rb	Yes
Abclonal	A1920	UMOD	Rb	Yes
Abclonal	A19707	VDAC1	Rb	Yes
Abcam	ab33168	VE-Cadherin	Rb	Yes
Abclonal	A19607	Vimentin	Rb	Yes
SYSY	443 005	VIP	Gp	Yes
AbClonal	A12531	VIP	Rb	Yes
Bioss	bs-0077R	VIP	Rb	Yes
AbClonal	A1335	VWF	Rb	Yes
SYSY	362 003	ZBTB20	Rb	Yes